

RICE UNIVERSITY

**Drogue Parachute Computational Structural and Fluid
Mechanics Analysis with Isogeometric Discretization**

by

Aaron Hartmann

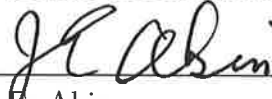
A THESIS SUBMITTED
IN PARTIAL FULFILLMENT OF THE
REQUIREMENTS FOR THE DEGREE

Master of Science

APPROVED, THESIS COMMITTEE:



T. E. Tezduyar, Chair
Professor of Mechanical Engineering



J. E. Akin
Professor of Mechanical Engineering and
Professor of Computational and Applied
Mathematics



A. J. Meade
Professor of Mechanical Engineering



K. Takizawa
Associate Professor in Department of
Modern Mechanical Engineering
Waseda University, Tokyo, Japan

HOUSTON, TEXAS

APRIL 2017

The views expressed in this thesis are those of the author and do not reflect the official policy or position of the United States Air Force, Department of Defense, or the U.S. Government.

Abstract

Drogue Parachute Computational Structural and Fluid Mechanics Analysis with Isogeometric Discretization

by

Aaron Hartmann

During the Orion spacecraft's return, at higher altitudes drogue parachutes will be used for deceleration. These parachutes are made of ribbons and have 24 gores, with 52 ribbons in each gore, where a gore is the slice of the parachute between two radial reinforcement cables extending from the parachute apex to the skirt. There are hundreds of gaps that the flow goes through, and there are also three wider gaps created by removing ribbons. Computational analysis can help reduce the number of costly drop tests in comprehensive evaluation of the parachute performance. Reliable analysis requires accurate computation of the parachute fluid–structure interaction (FSI) between the drogue and the compressible flow it is subjected to. The FSI computation is challenging because of the geometric and flow complexities and requires first creation of a starting parachute shape and flow field. This is a process that by itself is rather challenging, and that is what we are focusing on here. In our structural and fluid mechanics computations, for spatial discretization, we use isogeometric discretization with quadratic NURBS basis functions. This gives us a parachute shape that is smoother than what we get from a typical finite element discretization. In the flow analysis, we use the NURBS basis functions in the context of the compressible-flow Space–Time SUPG (ST SUPG) method. The combination of the ST framework,

NURBS basis functions, and the SUPG stabilization assures superior computational accuracy.

Acknowledgments

I would like to thank my advisor and mentor, Dr. Tayfun Tezduyar, for giving me the opportunity to attend Rice University as a member of T★AFSM. It has been a privilege to not only learn from him, but to work in his research group. In addition I would like to thank my co-advisor, Dr. Kenji Takizawa, and all of the help, support, and guidance he gave during my time at Rice University and writing my thesis. I would not be submitting a thesis if not for both of them, and I only hope someday I can work as tirelessly as they do everyday.

Thank you to Dr. Andrew Meade and Dr. Ed Akin for their time and effort serving as members of my thesis committee on top of their busy schedules.

I would like to show my gratitude to all the members of T★AFSM including previous members and those that I never had had the chance to meet or work with directly but keep the programs running smoothly. I would especially like to thank those I did work with directly: Taro Kanai, Takafumi Sasaki, Sen Mei, Linqi Pan, Ruochun Zhang, Yuxuan Yu, Reha Avsar, and Mingyuan Fu.

This work was supported in part by the Data Analysis and Visualization Cyberinfrastructure funded by NSF under grand OCI-0959097; NIH award NCRR S10RR02950, an IBM Shared University Research (SUR) Award in partnership with CISCO, Qlogic and Adaptive Computing; and Rice University.

Contents

Abstract	iii
Acknowledgments	v
List of Figures	viii
List of Tables	x
1 Introduction	1
2 Governing Equations and Porosity Models	5
2.1 Structural Mechanics	5
2.2 Fluid Mechanics	6
2.3 Porosity Model	7
2.3.1 Relationship between the fluid inside the media and the surrounding fluid	8
2.3.2 Mass flux	9
2.3.3 Momentum flux	11
2.3.4 Energy flux	11
3 Finite Element Formulations	12
3.1 Semi-discrete Formulation of Structural Mechanics	12
3.2 Compressible-Flow ST SUPG Method	13

3.3	Compressible-Flow ST-SI Method	14
3.3.1	ST-SI base version	15
3.3.2	ST-SI version where the SI is a fluid–solid interface with weakly- imposed flow velocity and temperature conditions	17
3.3.3	ST-SI version where the SI is a fluid–solid interface with weakly- imposed flow velocity and adiabatic conditions	18
3.3.4	ST-SI version where the SI is the interface between a thin porous structure and the surrounding fluid with weakly-imposed flow velocity and adiabatic conditions	20
4	Problem and Computational Setup	24
4.1	Drogue Parachute and Flight Conditions	24
4.2	Parachute Structure Computational Setup	26
4.3	Single-Gore Fluid Computational Setup	26
4.4	Full-Canopy Fluid Computational Setup	27
5	Computational Results	31
5.1	Parachute Structure Results	31
5.2	Single-Gore Fluid Results	35
5.3	Full-Canopy Fluid Results	40
6	Concluding Remarks	43
	Bibliography	44

List of Figures

2.1	Schematic representation a porous media. The coordinates x_B and x_A represent the “B” (“below”) and “A” (“above”) sides of the media. The flow direction from the B side to the A side is taken as the positive flow direction. The flow is only in the normal direction, and across the media, the mass flow rate is invariant and the pressure is continuous. The temperature-related condition will be described later.	7
4.1	Parachute configuration (from [35, 34])	25
4.2	Structural mechanics control mesh with 91, 612 control points (nn) and 19, 826 elememnts (ne)	26
4.3	Canopy fluid mechanics control mesh for AM31 single-gore fluid computations with 198, 112 control points (nn) and 111, 500 elements (ne), and a close-up view	28
4.4	Patch definition (from [35, 34])	28
4.5	Fluid mechanics control mesh for AM31 full-canopy fluid computations with 223, 934 control points (nn) and 116, 248 elements (ne), and a close-up view	30
5.1	Structural mechanics parachute deformations	32
5.2	Canopy shape from structural mechanics computations looking in the vertical direction	33

5.3	Canopy shape from structural mechanics computations looking in the y-direction	34
5.4	Patch-averaged values of $ \dot{m} $ through the gaps	36
5.5	Patch-averaged values of \mathcal{M}^2	36
5.6	Patch-averaged values of $ \dot{m} $, \mathcal{M}^2 , and \mathcal{M}^2 with the least-squares curve fitting lines where the dashed line for Patch 4 excludes the $\frac{\mu}{D}$ because it results in negative values for some \mathcal{M}^2	37
5.7	Comparison between using the parameters from the NURBS results and previous FEM results for \mathcal{M}^2 and $ \dot{m} $ for each patch with the NURBS results on the left and FEM results on the right	38
5.8	Velocity vectors around the canopy on a vertical slice plane scaled and colored to magnitude for AM31 using porosity parameters obtained from FEM on top and those obtained by NURBS below	40
5.9	Density around the canopy on a vertical slice plane for AM31 using porosity parameters obtained from FEM on top and those obtained by NURBS below	41
5.10	Pressure distribution above the canopy (left) and pressure distribution below the canopy (right) for AM31 using porosity parameters obtained from FEM on top and those obtained by NURBS below	42

List of Tables

4.1	Flight conditions	25
4.2	Number of control points (nn) and number of elements (ne) in meshes	29
5.1	Deformed parachute diameters	32
5.2	Fabric and geometric area ratios for each patch	34
5.3	Calculated geometric porosity parameters	36
5.4	Geometric porosity parameters from [34]	36
5.5	Porosity values from NURBS single-gore results	39
5.6	Porosity values from [34] applied to new NURBS mesh	39

Chapter 1

Introduction

Computational analysis has become an important aspect of most engineering work. However, even with widespread use and advanced computational techniques, research must continue to address shortcomings with current techniques and solve more complex problems in the future. One class of challenging problems that continues to be studied is fluid–structure interaction (FSI). In FSI problems, the fluid and structural mechanics are coupled together. The coupling leads to challenges in maintaining accuracy because of the moving interface, need to maintain mesh resolution near the surface, and the different computational properties between the solid and fluid calculations.

While the Team for Advanced Flow Simulation and Modeling (T★AFSM) has developed, brought to maturity, and used space–time (ST) methods to solve numerous FSI problems in the incompressible-flow regime, such as flapping wings, turbochargers, arteries, wind turbines and parachutes [32, 38, 33, 37, 35], compressible-flow FSI methods are not as mature and still require development. As interest in space continues to grow, companies and agencies seek various ways to make space travel more affordable, practical, safe, and useful. While there are several methods a spacecraft can use to decelerate and land, parachutes provide a relatively simple, economical,

and effective option, and more research into modeling parachutes can lead to better designs and reduce the amount of testing necessary in turn reducing costs.

The Orion spacecraft being developed by NASA will use parachutes to decelerate on its return to Earth. A cluster of three main parachutes will be deployed for the final descent but two drogue parachutes will be deployed at high speed for its initial deceleration and to stabilize it. These drogue parachutes must be able to handle the large forces required for slowing down and stabilizing the capsule over a large range of altitudes and Mach numbers up to 0.7 in order to safely and accurately land the Orion spacecraft and its crew. While NASA has completed some full-scale tests, computational analysis can further progress the design and safety of the parachutes so that the Orion spacecraft can safely carry its crew regardless of which planet it might be used.

In preparation for fully-coupled parachute FSI computations, which are particularly challenging because of the geometric and flow complexities, a deformed shape and developed flow must first be created, which in itself is a challenging problem that this thesis will address.

As explained in detail in [34], the core numerical technology used by the T★AFSM for parachute modeling is based on the Deforming-Spatial-Domain/Stabilized ST (DSD/SST) method [48, 49, 41, 43], which was upgraded in [51, 27]. The Streamline-Upwind/Petrov-Galerkin (SUPG) [9] and Pressure-Stabilizing/Petrov-Galerkin (PSPG) [41] methods are used as stabilization parts for the DSD/SST method, and for that the method is now called “ST-SUPS”. The variational multiscale version of the DSD/SST method includes turbulence modeling and is called the ST-VMS method [27, 29], where the VMS terms come from the residual-based VMS method [12, 3, 2].

Compressible-flow computational methods have been developed similar to the incompressible-flow methods described in the preceding paragraph. The core compressible-flow method is called ST SUPG method, which is the DSD/SST method for compressible-

flow [40, 56, 58, 57, 19, 34]. It combines the DSD/SST concept with the compressible-flow SUPG method [14]. The compressible-flow ST SUPG method includes shock-capturing like “YZ β ” shock-capturing [57, 58, 56, 19].

Parachutes pose particular challenges, which require special techniques. Many of these difficulties have been addressed through the use of specialized techniques beyond the core FSI methods. Some of these techniques include contact algorithms [51, 26], interface projection methods [51, 54, 25], gore curvature calculations [36], “disreefing” [22, 31], and parachute designs with modified “geometric porosity” [22, 30, 34].

Slip-interface (SI) techniques were first developed to deal with spinning solid surfaces to keep the high-resolution boundary layer mesh, but is useful in many areas such as being able to have nonmatching meshes at an interface, allowing for greater flexibility and in the use of porosity modeling [37]. The complex geometry of parachutes means there are hundreds of small gaps interspersed between patches of fabric that is permeable. Resolving the flow through every gap would be infeasible and require very large meshes and computational costs. Modeling the geometric porosity created by the gaps makes it possible to still compute the parachutes FSI with accuracy while greatly reducing the computational costs. Homogenized Modeling of Geometric Porosity (HMGP) [54, 22] is the method used by the T★AFSM, and a new version developed in [34]

Isogeometric Analysis (IGA) [13] has been progressing and the use of non-uniform rational B-spline (NURBS) basis functions has been adopted in both time and spatial dimensions. The methods are able to use higher-order functions including NURBS functions. With NURBS basis functions, we can represent the geometry more accurately, and possibly perfectly, which the standard finite elements fail to do. The usefulness of NURBS functions have already been demonstrated in accurately modeling flow problems [5, 4, 6].

The defining characteristic of FSI problems is the coupling between the fluid and

structure, and any FSI computation must control how to couple these and deal with mesh motion as well. The DSD/SST method first used block-iterative coupling for FSI (see [51, 45, 53] for the terminology) before progressing to quasi-direct and direct coupling [53] with additional improvements as well [51, 54, 59, 24, 25]. The progression to direct coupling and special techniques has enabled modeling complicated parachutes [54, 55, 59, 28, 25, 23, 39, 22]. Sequentially-coupled FSI (SCFSI) technique is a simple method for coupling, albeit useful method for progressing to fully-coupled FSI, where the structure and fluid are computed separately and then the results from either one are applied to the other to compute another round. This method is not as accurate as fully-coupled FSI, but it provides a good starting points for fully-coupled FSI without the limitations and resources necessary for fully-coupled FSI. The SCFSI technique has been used in parachute computations before [59, 39]. This thesis will examine some of the techniques described above, particularly porosity modeling in the compressible-flow regime using NURBS basis functions, as applied to the drogue parachute for the Orion spacecraft, to be used for starting parachute shape and flow field in fully-coupled FSI.

Chapters 2 and 3 cover governing equations and formulations for the computations in the thesis, starting with structural mechanics followed by fluid mechanics. The structural mechanics formulations are based on a semi-discrete formulation while the fluid mechanics are governed by Navier–Stokes equations of compressible flows and use the compressible-flow ST SUPG formulation. Chapter 4 describes the problem and computational setup including a description of the parachute and flight conditions used for the structural, single-gore fluid, and full-canopy fluid computations. Chapter 5 takes a look at the results of the computations and Chapter 6 provides some concluding remarks.

Chapter 2

Governing Equations and Porosity Models

2.1 Structural Mechanics

The material in this section is from [23].

Let $\Omega_t^s \subset \mathbb{R}^{n_{\text{xd}}}$ be the spatial domain with boundary Γ_t^s , where $n_{\text{xd}} = 3$ for the continuum element, $n_{\text{xd}} = 2$ for membranes, and $n_{\text{xd}} = 1$ for cables. The superscript “s” indicates the structure. The parts of Γ_t^s corresponding to the essential and natural boundary conditions are represented by $(\Gamma_t^s)_g$ and $(\Gamma_t^s)_h$. The equations of motion are written as

$$\rho^s \left(\frac{d^2 \mathbf{y}}{dt^2} + \eta \frac{d\mathbf{y}}{dt} - \mathbf{f}^s \right) - \nabla \cdot \boldsymbol{\sigma}^s = \mathbf{0}, \quad (2.1)$$

where ρ^s , \mathbf{y} , η , \mathbf{f}^s and $\boldsymbol{\sigma}^s$ are the material density, structural displacement, damping coefficient, external force and the Cauchy stress tensor, respectively. The stresses are expressed in terms of the second Piola–Kirchhoff stress tensor \mathbf{S} , which is related to the Cauchy stress tensor through a kinematic transformation. For the classes of FSI problems the T★AFSM has been focusing on, what makes one structural element

model different from the other is the manner in which \mathbf{S} is defined. These definitions can be found in earlier T★AFSM publications [51, 52, 28].

2.2 Fluid Mechanics

The material in this section is from [34].

Let $\Omega_t \subset \mathbb{R}^{n_{\text{sd}}}$ be the spatial domain with boundary Γ_t at time $t \in (0, T)$. The subscript t indicates the time-dependence of the domain. The symbols ρ , \mathbf{u} and p will represent the density, velocity and pressure, respectively, and $\boldsymbol{\varepsilon}(\mathbf{u}) = ((\nabla \mathbf{u}) + (\nabla \mathbf{u})^T) / 2$ is the strain-rate tensor. The stress tensor is defined as $\boldsymbol{\sigma}(\mathbf{u}, p) = -p\mathbf{I} + \mathbf{T}$, where \mathbf{I} is the identity tensor, and \mathbf{T} is the Newtonian viscous tensor: $\mathbf{T} = \lambda(\nabla \cdot \mathbf{u})\mathbf{I} + 2\mu\boldsymbol{\varepsilon}(\mathbf{u})$. Here λ and μ ($= \rho\nu$) are the viscosity coefficients, ν is the kinematic viscosity, and it is assumed that $\lambda = -2\mu/3$. The Navier–Stokes equations of compressible flows can be written on Ω_t and $\forall t \in (0, T)$ as

$$\frac{\partial \mathbf{U}}{\partial t} + \frac{\partial \mathbf{F}_i}{\partial x_i} - \frac{\partial \mathbf{E}_i}{\partial x_i} - \mathbf{R} = \mathbf{0}, \quad (2.2)$$

where $\mathbf{U} = (\rho, \rho u_1, \rho u_2, \rho u_3, \rho e)$ is the vector of conservation variables, e is the total energy per unit volume, and \mathbf{F}_i and \mathbf{E}_i are, respectively, the Euler and viscous flux vectors:

$$\mathbf{F}_i = \begin{pmatrix} u_i \rho \\ u_i \rho u_1 + \delta_{i1} p \\ u_i \rho u_2 + \delta_{i2} p \\ u_i \rho u_3 + \delta_{i3} p \\ u_i (\rho e + p) \end{pmatrix}, \quad \mathbf{E}_i = \begin{pmatrix} 0 \\ T_{i1} \\ T_{i2} \\ T_{i3} \\ -q_i + T_{ik} u_k \end{pmatrix}. \quad (2.3)$$

Here δ_{ij} are the components of \mathbf{I} , q_i are the components of the heat flux vector, and T_{ij} are the components of \mathbf{T} . The equation of state typically corresponds to the ideal

gas assumption. The term \mathbf{R} represents all other components that might enter the equations, including the external forces.

Equation (2.2) can further be written in the form

$$\frac{\partial \mathbf{U}}{\partial t} + \mathbf{A}_i \frac{\partial \mathbf{U}}{\partial x_i} - \frac{\partial}{\partial x_i} \left(\mathbf{K}_{ij} \frac{\partial \mathbf{U}}{\partial x_j} \right) - \mathbf{R} = \mathbf{0}, \quad (2.4)$$

where

$$\mathbf{A}_i = \frac{\partial \mathbf{F}_i}{\partial \mathbf{U}}, \quad \mathbf{K}_{ij} \frac{\partial \mathbf{U}}{\partial x_j} = \mathbf{E}_i. \quad (2.5)$$

The essential and natural boundary conditions for Eq. (2.4) are represented as $\mathbf{U} = \mathbf{G}$ on $(\Gamma_t)_G$ and $n_i \left(\mathbf{K}_{ij} \frac{\partial \mathbf{U}}{\partial x_j} \right) = \mathbf{H}$ on $(\Gamma_t)_H$, where $(\Gamma_t)_G$ and $(\Gamma_t)_H$ are complementary subsets of the boundary Γ_t , n_i are the components of the unit normal vector \mathbf{n} , and \mathbf{G} and \mathbf{H} are given functions. A function $\mathbf{U}_0(\mathbf{x})$ is specified as the initial condition.

2.3 Porosity Model

The material in this section is from [34].

Consider a porous media as shown in Figure 2.1. The flow is only in the normal

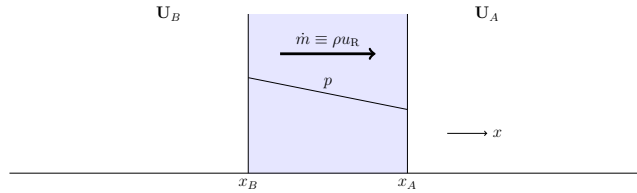


Figure 2.1: Schematic representation a porous media. The coordinates x_B and x_A represent the “B” (“below”) and “A” (“above”) sides of the media. The flow direction from the B side to the A side is taken as the positive flow direction. The flow is only in the normal direction, and across the media, the mass flow rate is invariant and the pressure is continuous. The temperature-related condition will be described later.

direction, and across the media, the mass flow rate is invariant and the pressure is continuous. The temperature-related condition will be described later. We assume

that, compared to the fluxes, the term

$$\frac{d}{dt} \left(\int_{x_B}^{x_A} \mathbf{U} dx \right) \quad (2.6)$$

is negligible. Then, the mass flow rate across the media,

$$\dot{m} = \rho u_R, \quad (2.7)$$

is constant. Here, u_R is the velocity relative to the porous media, which is only in the normal direction.

We assume that the pressure gradient can be expressed as

$$-\frac{dp}{dx} = \frac{\mu}{S} u_R + \frac{\rho}{L} u_R |u_R|, \quad (2.8)$$

where S and L are model parameters. This is known as the Darcy–Forchheimer model.

We assume a polytropic process in the media:

$$\rho = C p^{\frac{1}{n}}, \quad (2.9)$$

where n is the exponent constant, and C is a constant. This is general enough to cover most processes.

2.3.1 Relationship between the fluid inside the media and the surrounding fluid

Multiplying Eq. (2.8) with the density, we obtain

$$-\rho \frac{dp}{dx} = \text{sgn}(\dot{m}) \left(\frac{\mu}{S} |\dot{m}| + \frac{1}{L} |\dot{m}|^2 \right), \quad (2.10)$$

and using Eq. (2.9), we can integrate in the normal direction:

$$-\int_{x_B}^{x_A} C p^{\frac{1}{n}} \frac{dp}{dx} dx = \int_{x_B}^{x_A} \text{sgn}(\dot{m}) \left(\frac{\mu}{S} |\dot{m}| + \frac{1}{L} |\dot{m}|^2 \right) dx. \quad (2.11)$$

With the transformed model parameters defined as

$$D = \frac{S}{(x_A - x_B)}, \quad (2.12)$$

$$\frac{1}{\beta} = \frac{L}{(x_A - x_B)}, \quad (2.13)$$

the integration yields

$$-C \frac{n}{1+n} \left(p_A^{\frac{1+n}{n}} - p_B^{\frac{1+n}{n}} \right) = \text{sgn}(\dot{m}) \left(\frac{\mu}{D} |\dot{m}| + \beta |\dot{m}|^2 \right). \quad (2.14)$$

Substituting for C from Eq. (2.9), we obtain

$$-\frac{n}{1+n} (\rho_A p_A - \rho_B p_B) = \text{sgn}(\dot{m}) \left(\frac{\mu}{D} |\dot{m}| + \beta |\dot{m}|^2 \right). \quad (2.15)$$

2.3.2 Mass flux

We define \mathcal{M}^2 as

$$\mathcal{M}^2 \equiv -\frac{n}{1+n} (\rho_A p_A - \rho_B p_B) \text{sgn}(\dot{m}), \quad (2.16)$$

and because

$$\text{sgn}(\dot{m}) = -\text{sgn}(\rho_A p_A - \rho_B p_B), \quad (2.17)$$

the definition translates to

$$\mathcal{M}^2 \equiv \frac{n}{1+n} |\rho_A p_A - \rho_B p_B|. \quad (2.18)$$

With that, we rewrite Eq. (2.15) as

$$\beta |\dot{m}|^2 + \frac{\mu}{D} |\dot{m}| - \mathcal{M}^2 = 0, \quad (2.19)$$

and this is the equation we solve for $|\dot{m}|$. We obtain

$$|\dot{m}| = \frac{-\frac{\mu}{D} + \sqrt{\left(\frac{\mu}{D}\right)^2 + 4\beta\mathcal{M}^2}}{2\beta} \quad (2.20)$$

for $\beta \neq 0$, and the form

$$|\dot{m}| = \frac{2\mathcal{M}^2}{\frac{\mu}{D} + \sqrt{\left(\frac{\mu}{D}\right)^2 + 4\beta\mathcal{M}^2}} \quad (2.21)$$

would be applicable also when $\beta = 0$. From that, we can get

$$\dot{m} = -\frac{2\mathcal{M}^2}{\frac{\mu}{D} + \sqrt{\left(\frac{\mu}{D}\right)^2 + 4\beta\mathcal{M}^2}} \text{sgn}(\rho_A p_A - \rho_B p_B). \quad (2.22)$$

Remark 1 *Setting $n = \gamma$ gives us \mathcal{M}^2 for adiabatic process:*

$$\mathcal{M}^2 = \frac{\gamma}{1+\gamma} |\rho_A p_A - \rho_B p_B|. \quad (2.23)$$

Remark 2 *Setting $n = \infty$ gives us \mathcal{M}^2 for incompressible-flow process:*

$$\mathcal{M}^2 = \rho |p_A - p_B|. \quad (2.24)$$

2.3.3 Momentum flux

The force acting on the fluid per unit area due to the media, \mathbf{h}_M , is expressed in terms of the momentum-conservation fluxes on the two sides:

$$(\dot{m}\mathbf{u}_A + p_A) - (\dot{m}\mathbf{u}_B + p_B) = \mathbf{h}_M. \quad (2.25)$$

2.3.4 Energy flux

Neglecting the energy exchange due to viscous forces, the heat leaving from the fluid to the media, q_M , is expressed in terms of the energy-conservation fluxes on the two sides:

$$\left(\dot{m} \left(e_A + \frac{p_A}{\rho_A} \right) + \mathbf{n} \cdot \mathbf{q}_A \right) - \left(\dot{m} \left(e_B + \frac{p_B}{\rho_B} \right) + \mathbf{n} \cdot \mathbf{q}_B \right) = -q_M, \quad (2.26)$$

where the unit normal vector \mathbf{n} is pointing from the B side to the A side. Heat flux condition between a thin porous structure and the surrounding fluid specifies q_M to a given value. As a special case of that, the adiabatic condition between a thin porous structure and the surrounding fluid specifies q_M to zero.

Chapter 3

Finite Element Formulations

3.1 Semi-discrete Formulation of Structural Mechanics

The material in this section is from [23].

With \mathbf{y}^h and \mathbf{w}^h coming from appropriately defined trial and test function spaces, respectively, the semi-discrete finite element formulation of the structural mechanics equations (see [17, 8, 21]) is written as

$$\int_{\Omega_0^s} \mathbf{w}^h \cdot \rho^s \frac{d^2 \mathbf{y}^h}{dt^2} d\Omega + \int_{\Omega_0^s} \mathbf{w}^h \cdot \eta \rho^s \frac{d\mathbf{y}^h}{dt} d\Omega + \int_{\Omega_0^s} \delta \mathbf{E}^h : \mathbf{S} d\Omega = \int_{\Omega_t^s} \mathbf{w}^h \cdot (\mathbf{t}^h + \rho^s \mathbf{f}^s) d\Omega. \quad (3.1)$$

The fluid mechanics forces acting on the structure are represented by vector \mathbf{t}^h . The above formulation is for structures represented by a membrane model. The left-hand-side terms of Eq. (3.1) are referred to in the original configuration and the right-hand-side terms in the deformed configuration at time t . Time discretization of Eq. (3.1) is based on the Hilber–Hughes–Taylor scheme [11].

Remark 3 *In the computations reported here and those reported earlier by the T★AFSM, the mass matrix associated with the first term of Eq. (3.1) is lumped.*

3.2 Compressible-Flow ST SUPG Method

The material in this section is from [34].

The compressible-flow ST SUPG method is essentially the same as the compressible-flow DSD/SST method, but without necessarily implying a mesh motion. The compressible-flow DSD/SST method is a straightforward mixture of the DSD/SST concept and the compressible-flow SUPG method. The compressible-flow SUPG method [50, 14, 16, 15] was introduced in 1982 and evolved over the years (see Chapter 1). The DSD/SST method [41, 43, 51, 27, 29, 7], introduced in 1990, also evolved over the years (see Chapter 1 and [7]).

In the DSD/SST method, the finite element formulation is written over a sequence of N ST slabs Q_n , where Q_n is the slice of the ST domain between the time levels t_n and t_{n+1} . The lateral boundary P_n will have complementary subsets where essential and natural boundary conditions are enforced, just like how it is with Γ_t . At each time step, the integrations are performed over Q_n . The functions are continuous within an ST slab, but discontinuous from one ST slab to another, and the superscripts “−” and “+” will indicate the values of the functions just below and just above the time level. The trial solution and test function spaces are defined over Q_n by using ST polynomials that are typically first-order, but sometimes higher-order. Each Q_n is decomposed into elements Q_n^e , where $e = 1, 2, \dots, (n_{el})_n$. The subscript n used with n_{el} is for the general case where the number of ST elements may change from one ST slab to another.

We assume that we have constructed some suitably-defined finite-dimensional trial solution and test function spaces $(\mathcal{S}_U^h)_n$ and $(\mathcal{V}_U^h)_n$. The DSD/SST formulation [47,

42, 44, 46, 56, 57, 58, 18] of Eq. (2.4) can be written as follows: given $(\mathbf{U}^h)_n^-$, find $\mathbf{U}^h \in (\mathcal{S}_U^h)_n$, such that $\forall \mathbf{W}^h \in (\mathcal{V}_U^h)_n$:

$$\begin{aligned}
& \int_{Q_n} \mathbf{W}^h \cdot \left(\frac{\partial \mathbf{U}^h}{\partial t} + \mathbf{A}_i^h \frac{\partial \mathbf{U}^h}{\partial x_i} - \mathbf{R}^h \right) dQ \\
& + \int_{Q_n} \frac{\partial \mathbf{W}^h}{\partial x_i} \cdot \mathbf{K}_{ij}^h \frac{\partial \mathbf{U}^h}{\partial x_j} dQ - \int_{(P_n)_H} \mathbf{W}^h \cdot \mathbf{H}^h dP \\
& + \int_{\Omega_n} (\mathbf{W}^h)_n^+ \cdot ((\mathbf{U}^h)_n^+ - (\mathbf{U}^h)_n^-) d\Omega \\
& + \sum_{e=1}^{(n_{el})_n} \int_{Q_n^e} \boldsymbol{\tau}_{\text{SUPG}} \left(\frac{\partial \mathbf{W}^h}{\partial t} + \frac{\partial \mathbf{W}^h}{\partial x_k} \mathbf{A}_k^h \right) \cdot \mathbf{R}_A(\mathbf{U}^h) dQ \\
& + \sum_{e=1}^{(n_{el})_n} \int_{Q_n^e} \nu_{\text{SHOC}} \frac{\partial \mathbf{W}^h}{\partial x_i} \cdot \frac{\partial \mathbf{U}^h}{\partial x_i} dQ = 0, \tag{3.2}
\end{aligned}$$

where

$$\mathbf{R}_A(\mathbf{U}^h) = \frac{\partial \mathbf{U}^h}{\partial t} + \mathbf{A}_i^h \frac{\partial \mathbf{U}^h}{\partial x_i} - \frac{\partial}{\partial x_i} \left(\mathbf{K}_{ij}^h \frac{\partial \mathbf{U}^h}{\partial x_j} \right) - \mathbf{R}^h, \tag{3.3}$$

$\boldsymbol{\tau}_{\text{SUPG}}$ is the SUPG stabilization matrix, and ν_{SHOC} is the shock-capturing parameter. The stabilization is residual-based because the residual of the compressible-flow equations, $\mathbf{R}_A(\mathbf{U}^h)$, appears as a factor in the stabilization term. We start with $(\mathbf{U}^h)_0^- = \mathbf{U}_0(\mathbf{x})$ and apply the formulation sequentially to all ST slabs $Q_0, Q_1, Q_2, \dots, Q_{N-1}$.

3.3 Compressible-Flow ST-SI Method

The material in this section is from [34].

3.3.1 ST-SI base version

First we define a new function and introduce a notation based on that:

$$\mathcal{F}(\mathbf{U}) = n_i \mathbf{F}_i(\mathbf{U}) - n_i v_i \mathbf{U}, \quad (3.4)$$

$$\mathcal{F}^h = \mathcal{F}(\mathbf{U}^h), \quad (3.5)$$

where \mathbf{v} is the mesh velocity and v_i is its i th component. In the ST-SI method associated with the formulation given by Eq. (3.2), we will have added boundary terms corresponding to the SI. We will use the labels “Side A” and “Side B” to represent the two sides of the SI. The boundary terms for the two sides will first be added separately, using test functions \mathbf{W}_A^h and \mathbf{W}_B^h . Then, putting together the terms added for each side, the complete set of terms added will be obtained. We give the boundary terms for only Side B:

$$\begin{aligned} & - \int_{(P_n)_{\text{SI}}} \mathbf{W}_B^h \cdot \mathcal{F}_B^h \, dP \\ & + \int_{(P_n)_{\text{SI}}} \mathbf{W}_B^h \cdot \frac{1}{2} (\mathcal{F}_B^h + \mathcal{F}_A^h + \alpha^h (\mathbf{U}_B^h - \mathbf{U}_A^h)) \, dP \\ & - \int_{(P_n)_{\text{SI}}} \mathbf{W}_B^h \cdot \frac{1}{2} (n_B^h)_i ((\mathbf{E}_B^h)_i + (\mathbf{E}_A^h)_i) \, dP \\ & - \gamma_{\text{ACI}} \int_{(P_n)_{\text{SI}}} \frac{\partial \mathbf{W}_B^h}{\partial x_j} \cdot \frac{1}{2} (n_B^h)_i \left((\mathbf{K}_B^h)_{ij}^T + (\mathbf{K}_A^h)_{ij}^T \right) (\mathbf{U}_B^h - \mathbf{U}_A^h) \, dP \\ & + \int_{(P_n)_{\text{SI}}} \mathbf{W}_B^h \cdot \frac{\mathbf{C}^h}{h} (\mathbf{U}_B^h - \mathbf{U}_A^h) \, dP, \end{aligned} \quad (3.6)$$

where

$$\alpha^h = \max \left(|\mathbf{n}_B^h \cdot (\mathbf{u}_B^h - \mathbf{v}^h)| + c_B^h, |\mathbf{n}_A^h \cdot (\mathbf{u}_A^h - \mathbf{v}^h)| + c_A^h \right), \quad (3.7)$$

$$h = \min(h_B, h_A), \quad (3.8)$$

$$h_B = 2 \left(\sum_{\alpha=1}^{n_{\text{ent}}} \sum_{a=1}^{n_{\text{ens}}} |\mathbf{n}_B \cdot \nabla N_a^\alpha| \right)^{-1} \quad (\text{for Side B}), \quad (3.9)$$

$$h_A = 2 \left(\sum_{\alpha=1}^{n_{\text{ent}}} \sum_{a=1}^{n_{\text{ens}}} |\mathbf{n}_A \cdot \nabla N_a^\alpha| \right)^{-1} \quad (\text{for Side A}). \quad (3.10)$$

Here, $(P_n)_{\text{SI}}$ is the SI in the ST domain, c is the acoustic speed, n_{ens} and n_{ent} are the number of spatial and temporal element nodes, N_a^α is the basis function associated with spatial and temporal nodes a and α , and \mathbf{C}^h is a tensor that will be defined later. Side A counterpart of Eq. (3.6) can be written by just interchanging subscripts A and B.

Remark 4 *The first and second integrations set the Euler flux at the boundary to the Lax–Friedrichs flux.*

Remark 5 *The third integration contains the average viscous terms.*

Remark 6 *The fourth integration, with $\gamma_{\text{ACI}} = 1$, is the adjoint consistency term introduced in the symmetric-interior-penalty discontinuous Galerkin method [1]. The other choice is $\gamma_{\text{ACI}} = -1$, resulting in a method that is adjoint inconsistent, which is known as the nonsymmetric-interior-penalty discontinuous Galerkin method [20].*

Remark 7 *The fifth integration is a penalty-like term. Several forms of the tensor \mathbf{C}^h have been proposed and we use the one from [10]:*

$$\mathbf{C}^h = \frac{C}{2} (n_B^h)_i (n_B^h)_j \left((\mathbf{K}_B^h)_{ij} + (\mathbf{K}_A^h)_{ij} \right), \quad (3.11)$$

where C is a nondimensional positive constant, which is 1.0 in the computations reported in this article.

Putting together the boundary terms added for each side, the complete set of terms added becomes

$$\begin{aligned}
& \int_{(P_n)_{\text{SI}}} (\mathbf{W}_B^h - \mathbf{W}_A^h) \cdot \frac{1}{2} (\mathcal{F}_A^h - \mathcal{F}_B^h - \alpha^h (\mathbf{U}_A^h - \mathbf{U}_B^h)) \, dP \\
& - \int_{(P_n)_{\text{SI}}} \left((n_B^h)_i \mathbf{W}_B^h + (n_A^h)_i \mathbf{W}_A^h \right) \cdot \frac{1}{2} \left((\mathbf{E}_B^h)_i + (\mathbf{E}_A^h)_i \right) \, dP \\
& - \gamma_{\text{ACI}} \int_{(P_n)_{\text{SI}}} \left((n_B^h)_i \frac{\partial \mathbf{W}_B^h}{\partial x_j} - (n_A^h)_i \frac{\partial \mathbf{W}_A^h}{\partial x_j} \right) \cdot \frac{1}{2} \left((\mathbf{K}_B^h)_{ij}^T + (\mathbf{K}_A^h)_{ij}^T \right) (\mathbf{U}_B^h - \mathbf{U}_A^h) \, dP \\
& + \int_{(P_n)_{\text{SI}}} (\mathbf{W}_B^h - \mathbf{W}_A^h) \cdot \frac{\mathbf{C}^h}{h} (\mathbf{U}_B^h - \mathbf{U}_A^h) \, dP. \tag{3.12}
\end{aligned}$$

3.3.2 ST-SI version where the SI is a fluid–solid interface with weakly-imposed flow velocity and temperature conditions

The boundary terms added for Side B are given as

$$\begin{aligned}
& - \int_{(P_n)_{\text{SI}}} \mathbf{W}_B^h \cdot \mathcal{F}_B^h \, dP \\
& + \int_{(P_n)_{\text{SI}}} \mathbf{W}_B^h \cdot \mathcal{F}(\mathbf{G}_{\text{ISO}}^h) \, dP \\
& - \int_{(P_n)_{\text{SI}}} \mathbf{W}_B^h \cdot (n_B^h)_i (\mathbf{E}_B^h)_i \, dP \\
& - \gamma_{\text{ACI}} \int_{(P_n)_{\text{SI}}} \frac{\partial \mathbf{W}_B^h}{\partial x_j} \cdot (n_B^h)_i (\mathbf{K}_B^h)_{ij}^T (\mathbf{U}_B^h - \mathbf{G}_{\text{ISO}}^h) \, dP \\
& + \int_{(P_n)_{\text{SI}}} \mathbf{W}_B^h \cdot \frac{\mathbf{C}_{\text{ISO}}^h}{h} (\mathbf{U}_B^h - \mathbf{G}_{\text{ISO}}^h) \, dP, \tag{3.13}
\end{aligned}$$

where

$$\mathbf{G}_{\text{ISO}}^h = \begin{pmatrix} \rho_B^h \\ \rho_B^h g_1^h \\ \rho_B^h g_2^h \\ \rho_B^h g_3^h \\ \rho_B^h \left(C_v g_\theta^h + \frac{1}{2} \|\mathbf{g}^h\|^2 \right) \end{pmatrix}, \quad (3.14)$$

$$\mathbf{C}_{\text{ISO}}^h = C (n_B^h)_i (n_B^h)_j \left((\mathbf{K}_B^h)_{ij} \right), \quad (3.15)$$

and \mathbf{g}^h and g_θ^h are given functions.

3.3.3 ST-SI version where the SI is a fluid–solid interface with weakly-imposed flow velocity and adiabatic conditions

The boundary terms added for Side B are given as

$$\begin{aligned} & - \int_{(P_n)_{\text{SI}}} \mathbf{W}_B^h \cdot \mathcal{F}_B^h dP \\ & + \int_{(P_n)_{\text{SI}}} \mathbf{W}_B^h \cdot \mathcal{F}(\mathbf{G}_{\text{ADI}}^h) dP \\ & - \int_{(P_n)_{\text{SI}}} \mathbf{W}_B^h \cdot (n_B^h)_i \left((\mathbf{E}_B^h)_{\text{ADI}} \right)_i dP \\ & - \gamma_{\text{ACI}} \int_{(P_n)_{\text{SI}}} \frac{\partial \mathbf{W}_B^h}{\partial x_j} \cdot (n_B^h)_i \left(((\mathbf{K}_B^h)_{\text{ADI}})_{ij} \right)^T (\mathbf{U}_B^h - \mathbf{G}_{\text{ADI}}^h) dP \\ & + \int_{(P_n)_{\text{SI}}} \mathbf{W}_B^h \cdot \frac{\mathbf{C}_{\text{ADI}}^h}{h} (\mathbf{U}_B^h - \mathbf{G}_{\text{ADI}}^h) dP, \end{aligned} \quad (3.16)$$

where

$$((\mathbf{E}_B^h)_{\text{ADI}})_i = (\mathbf{E}_B^h)_i + \begin{pmatrix} 0 \\ 0 \\ 0 \\ 0 \\ (q_B^h)_i \end{pmatrix}, \quad (3.17)$$

$$((\mathbf{K}_B^h)_{\text{ADI}})_{ij} = (\mathbf{K}_B^h)_{ij} + \begin{pmatrix} \mathbf{0}^T \\ \mathbf{0}^T \\ \mathbf{0}^T \\ \mathbf{0}^T \\ \left(\frac{\partial q_i}{\partial \mathbf{U}_{,j}}\right)_B \end{pmatrix}, \quad (3.18)$$

$$\mathbf{G}_{\text{ADI}}^h = \begin{pmatrix} \rho_B^h \\ \rho_B^h g_1^h \\ \rho_B^h g_2^h \\ \rho_B^h g_3^h \\ \rho_B^h \left(C_v \theta_B^h + \frac{1}{2} \|\mathbf{g}^h\|^2 \right) \end{pmatrix}, \quad (3.19)$$

$$\mathbf{C}_{\text{ADI}}^h = C (n_B^h)_i (n_B^h)_j \left(((\mathbf{K}_B^h)_{\text{ADI}})_{ij} \right), \quad (3.20)$$

and \mathbf{g}^h is a given function. Note that $\mathbf{U}_{,j} = \frac{\partial \mathbf{U}}{\partial x_j}$.

3.3.4 ST-SI version where the SI is the interface between a thin porous structure and the surrounding fluid with weakly-imposed flow velocity and adiabatic conditions

In general, the adiabatic condition ($q_M = 0$) between the thin structure and the surrounding fluid implies

$$-\kappa \mathbf{n} \cdot \nabla \theta|_B = -\kappa \mathbf{n} \cdot \nabla \theta|_A. \quad (3.21)$$

As a special case of that, we might have

$$-\kappa \mathbf{n} \cdot \nabla \theta|_B = 0, \quad (3.22)$$

$$-\kappa \mathbf{n} \cdot \nabla \theta|_A = 0. \quad (3.23)$$

Special case

From Eq. (2.22) with Eq. (2.23), we obtain the mass flux as a function of the two conservation variables:

$$\dot{m}_B = \dot{m}(\mathbf{U}_B, \mathbf{U}_A). \quad (3.24)$$

The boundary terms added for Side B are given as

$$\begin{aligned} & - \int_{(P_n)_{SI}} \mathbf{W}_B^h \cdot \mathcal{F}_B^h dP \\ & + \int_{(P_n)_{SI}} \mathbf{W}_B^h \cdot \mathcal{D}(\mathbf{U}_B^h, \mathbf{U}_A^h) dP - \int_{(P_n)_{SI}} \mathbf{W}_B^h \cdot \boldsymbol{\varepsilon}_{VIS}(\mathbf{U}_B^h) dP \\ & - \gamma_{ACI} \int_{(P_n)_{SI}} \frac{\partial \mathbf{W}_B^h}{\partial x_j} \cdot \left((\boldsymbol{\kappa}_{VIS})_j^T(\mathbf{U}_B^h) \right) \cdot (\mathbf{U}_B^h - \mathbf{G}_{PORO}(\mathbf{U}_B^h, \mathbf{U}_A^h)) dP \\ & + \int_{(P_n)_{SI}} \mathbf{W}_B^h \cdot \frac{\mathbf{C}_{PORO}(\mathbf{U}_B^h, \mathbf{U}_A^h)}{h} (\mathbf{U}_B^h - \mathbf{G}_{PORO}(\mathbf{U}_B^h, \mathbf{U}_A^h)) dP. \end{aligned} \quad (3.25)$$

Here the normal components of the Euler flux vectors are taken as

$$\mathcal{D}(\mathbf{U}_B, \mathbf{U}_A) = \begin{pmatrix} \dot{m}_B \\ \dot{m}_B \left(\frac{\dot{m}_B}{\rho_B} \mathbf{n}_B + \mathbf{v} \right) + \mathbf{n}_B p_B \\ \frac{1}{2} (\mathcal{F}_e(\mathbf{U}_B, \dot{m}_B) + \mathcal{F}_e(\mathbf{U}_A, \dot{m}_B)) \\ + |\dot{m}_B| (g_e(\mathbf{U}_B, \dot{m}_B) - g_e(\mathbf{U}_A, \dot{m}_B)) + \mathbf{n}_B \cdot \mathbf{v} p_B \end{pmatrix}, \quad (3.26)$$

where

$$\mathcal{F}_e(\mathbf{U}, \dot{m}_B) = \dot{m}_B \left(g_e(\mathbf{U}, \dot{m}_B) + \frac{p}{\rho} \right), \quad (3.27)$$

$$g_e(\mathbf{U}, \dot{m}_B) = e - \frac{1}{2} \|\mathbf{u}\|^2 + \frac{1}{2} \left\| \frac{\dot{m}_B}{\rho} \mathbf{n} + \mathbf{v} \right\|^2. \quad (3.28)$$

The normal components of the viscous flux vectors, not including the heat conduction flux, are taken as

$$\mathcal{E}_{\text{VIS}}(\mathbf{U}) = \begin{pmatrix} 0 \\ \mathbf{h}_T(\mathbf{U}) \\ \mathbf{h}_T(\mathbf{U}) \cdot \mathbf{v} \end{pmatrix}, \quad (3.29)$$

where

$$\mathbf{h}_T(\mathbf{U}) = (\mathbf{I} - \mathbf{nn}) (\mathbf{n} \cdot \mathbf{T}). \quad (3.30)$$

The vectors and tensors involved in the fourth and fifth integrations of Eq. (3.25) are given as

$$(\mathcal{K}_{\text{VIS}})_j(\mathbf{U}) = (\delta_{jk} - n_j n_k) n_i (\mathbf{K}_{\text{ADI}})_{ik}, \quad (3.31)$$

$$\mathbf{G}_{\text{PORO}}(\mathbf{U}_B, \mathbf{U}_A) = \begin{pmatrix} \rho_B \\ \dot{m}_B \mathbf{n}_B + \rho_B \mathbf{v} \\ \rho_B g_e(\mathbf{U}_B, \dot{m}_B) \end{pmatrix}, \quad (3.32)$$

$$\mathbf{C}_{\text{PORO}}(\mathbf{U}_B, \mathbf{U}_A) = C(n_B)_i (n_B)_j ((\mathbf{K}_B)_{\text{ADI}})_{ij}. \quad (3.33)$$

General case

The boundary terms added for Side B are given as

$$\begin{aligned} & - \int_{(P_n)_{\text{SI}}} \mathbf{W}_B^h \cdot \mathcal{F}_B^h dP \\ & + \int_{(P_n)_{\text{SI}}} \mathbf{W}_B^h \cdot \mathcal{D}(\mathbf{U}_B^h, \mathbf{U}_A^h) dP \\ & - \int_{(P_n)_{\text{SI}}} \mathbf{W}_B^h \cdot \left(\boldsymbol{\varepsilon}_{\text{VIS}}(\mathbf{U}_B^h) \right. \\ & \quad \left. + \frac{1}{\rho_B^h + \rho_A^h} (\rho_B^h \boldsymbol{\varepsilon}_{\text{HEA}}(\mathbf{U}_B^h) - \rho_A^h \boldsymbol{\varepsilon}_{\text{HEA}}(\mathbf{U}_A^h)) \right) dP \\ & - \gamma_{\text{ACI}} \int_{(P_n)_{\text{SI}}} \frac{\partial \mathbf{W}_B^h}{\partial x_j} \cdot \left((\boldsymbol{\kappa}_{\text{VIS}})^T_j(\mathbf{U}_B^h) + \frac{1}{\rho_B^h + \rho_A^h} (\rho_B^h (\boldsymbol{\kappa}_{\text{HEA}})^T_j(\mathbf{U}_B^h) \right. \\ & \quad \left. - \rho_A^h (\boldsymbol{\kappa}_{\text{HEA}})^T_j(\mathbf{U}_A^h)) \right) \cdot (\mathbf{U}_B^h - \tilde{\mathbf{G}}_{\text{PORO}}(\mathbf{U}_B^h, \mathbf{U}_A^h)) dP \\ & + \int_{(P_n)_{\text{SI}}} \mathbf{W}_B^h \cdot \frac{\tilde{\mathbf{C}}_{\text{PORO}}(\mathbf{U}_B^h, \mathbf{U}_A^h)}{h} (\mathbf{U}_B^h - \tilde{\mathbf{G}}_{\text{PORO}}(\mathbf{U}_B^h, \mathbf{U}_A^h)) dP, \end{aligned} \quad (3.34)$$

where the normal component of the heat conduction part of the viscous flux vectors are taken as

$$\boldsymbol{\varepsilon}_{\text{HEA}}(\mathbf{U}) = \begin{pmatrix} 0 \\ \mathbf{0} \\ -\mathbf{n} \cdot \mathbf{q} \end{pmatrix}. \quad (3.35)$$

The vectors and tensors involved in the fourth and fifth integrations of Eq. (3.34) are given as

$$(\boldsymbol{\kappa}_{\text{HEA}})_j(\mathbf{U}) = \begin{pmatrix} \mathbf{0}^T \\ \mathbf{0}^T \\ \mathbf{0}^T \\ \mathbf{0}^T \\ -n_i \frac{\partial q_i}{\partial \mathbf{U}_j} \end{pmatrix}, \quad (3.36)$$

$$\tilde{\mathbf{G}}_{\text{PORO}}(\mathbf{U}_B, \mathbf{U}_A) = \begin{pmatrix} \rho_B \\ \dot{m}_B \mathbf{n}_B + \rho_B \mathbf{v} \\ \rho_B \left(g_e(\mathbf{U}_A, \dot{m}_A) + \frac{p_A}{\rho_A} - \frac{p_B}{\rho_B} \right) \end{pmatrix}, \quad (3.37)$$

$$\begin{aligned} \tilde{\mathbf{C}}_{\text{PORO}}(\mathbf{U}_B, \mathbf{U}_A) = & C (n_B)_j \left((n_B)_i ((\mathbf{K}_B)_{\text{ADI}})_{ij} \right. \\ & \left. + \frac{1}{\rho_B + \rho_A} \left(\rho_B (\boldsymbol{\kappa}_{\text{HEA}})_j(\mathbf{U}_B) - \rho_A (\boldsymbol{\kappa}_{\text{HEA}})_j(\mathbf{U}_A) \right) \right). \end{aligned} \quad (3.38)$$

Chapter 4

Problem and Computational Setup

4.1 Drogue Parachute and Flight Conditions

The material in this section is taken in part from [35, 34].

The Orion drogue parachute is a Variable Porosity Conical Ribbon parachute with a nominal diameter of 23 ft. Each of its 24 gores are made up of 52 2-inch ribbons that are kept closely spaced by seven parallel, equidistant vertical tapes. The primary longitudinal stiffness comes from the ribbon ends which are stitched to the radial lines. A vent band connects the 24 radial lines at the vent. The configuration can be seen in Figure 4.1.

The spacing between the horizontal ribbons is varied starting at 0.3 inches for the first 13 ribbons closest to the vent. The subsequent groups of 13 ribbons are spaced 0.4, 0.5, and 0.6 inches apart, respectively. Stability of the parachute is increased by removing ribbons in three locations. The ribbons are modeled with membrane elements. The upper, middle, and lower ribbons have slightly different material properties which were provided by NASA. The remaining lines, tapes, and bands are modeled with cable elements with varying properties depending on their actual function.

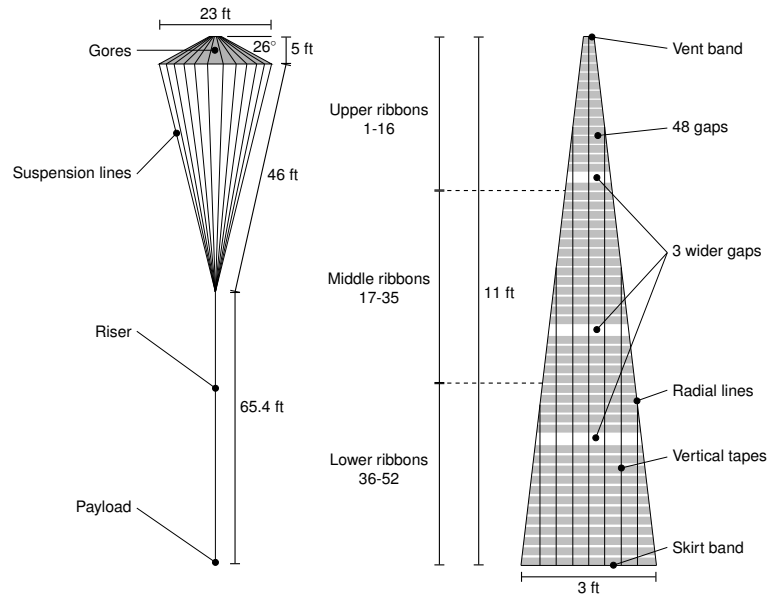


Figure 4.1: Parachute configuration (from [35, 34])

The parachute is designed to deploy over a large range of altitudes and speeds, so three altitudes: 10,000, 20,000 and 35,000 ft, and three Mach numbers: 0.3, 0.5 and 0.7 were chosen for modeling resulting in a total of nine different flight conditions referred to as AM11–AM33, where the first digit denotes the altitude and the second denotes the Mach number. Standard-day air properties are assumed for each flight condition and the relevant properties can be seen in Table 4.1.

Table 4.1: Flight conditions

AM (-)	Altitude (ft)	θ_∞ (K)	ρ_∞ (kg/m ³)	μ_∞ (Pa · s)	M_∞ (-)	$\ \mathbf{u}_\infty\ $ (m/s)	$\frac{1}{2}\rho_\infty\ \mathbf{u}_\infty\ ^2$ (Pa)
11	10,000	268	0.90	1.69×10^{-5}	0.3	98.5	4,386
12					0.5	164.2	12,185
13					0.7	229.9	23,882
21	20,000	249	0.65	1.59×10^{-5}	0.3	94.8	2,931
22					0.5	158.0	8,141
23					0.7	221.2	15,957
31	35,000	218	0.38	1.43×10^{-5}	0.3	88.9	1,500
32					0.5	148.2	4,166
33					0.7	207.5	8,166

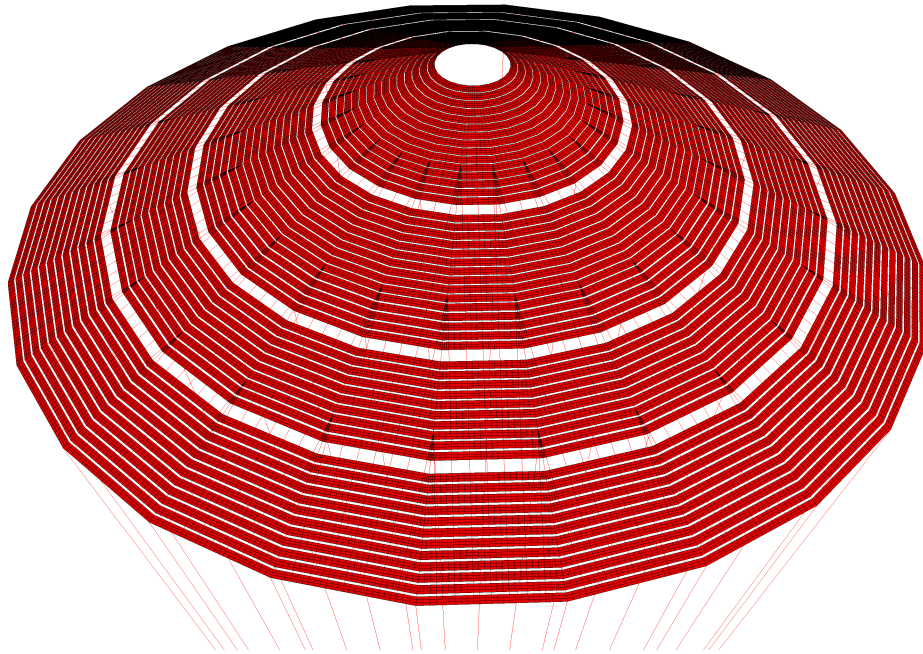


Figure 4.2: Structural mechanics control mesh with 91,612 control points (nn) and 19,826 elements (ne)

4.2 Parachute Structure Computational Setup

The structural mechanics mesh, shown in Figure 4.2, has 91,612 control points with 19,826 cubic NURBS elements. The elements are further divided into 6,648 membrane elements, 13,177 cable elements, and 1 payload element. A uniform pressure equal to the free-stream dynamic pressures in Table 4.1 is applied to the structure to deform the structure while fixing the payload element. The computations are run until a steady-state solution is obtained with 100 GMRES iterations, 4 nonlinear iterations, and a time step size of 0.001 s.

4.3 Single-Gore Fluid Computational Setup

The single-gore fluid mechanics mesh, shown in Figure 4.3 is built around the deformed structure shape obtained from the structural mechanics computations from flight condition AM31 with resolved gaps. The mesh consists of 198,112 control points

making 111,500 quadratic NURBS elements. In the radial direction, the ribbons are covered by 4 elements, the gap by 2 elements, and the missing ribbons by 6 elements. There are 9 elements in the circumferential direction of the gore.

A slip interface is placed away from the parachute interface with nonmatching interfaces so the number of control points and elements can be reduced and the total number of control points and elements for the mesh kept within reason. The mesh is moved using a separate structural mechanics computation to obtain meshes for the other flight conditions.

The free-stream velocity and temperature are prescribed at the inflow, zero stress and heat flux at the outflow, and weak slip and zero heat flux on the side boundaries. The fabric porosity of 40 CFM is modeled using Eqs. (2.19) and (2.23) where the β term equals zero because of the fully resolved gaps, and Sutherland's Law is used to model viscosity. Flight condition AM31 is computed first and later flight conditions use previous results as initial data to decrease the time for each computation. Computations are run with GMRES iterations starting with 10 and increasing to 60 later, 3 nonlinear iterations, and time step sizes of 2.0×10^{-5} for AM31 and 2.0×10^{-4} s for AM11 and AM32. Only flight conditions AM11, AM31, and AM32 were completed for this thesis.

4.4 Full-Canopy Fluid Computational Setup

The full-canopy fluid mechanics mesh, shown in Figure 4.5 is built in a similar way as the single-gore mesh if it was rotated 24 times to make a full canopy, but the gaps are not full resolved. Instead they are combined into four patches as shown in Figure 4.4. The mesh consists of 223,934 control points forming 116,248 quadratic NURBS elements.

A slip interface is placed away from the parachute interface and in the center

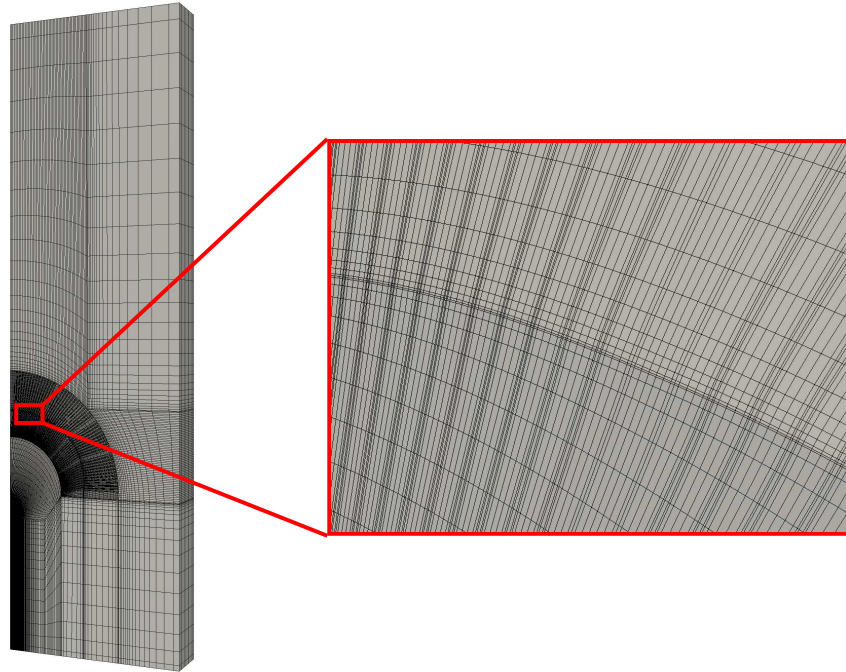


Figure 4.3: Canopy fluid mechanics control mesh for AM31 single-gore fluid computations with 198,112 control points (nn) and 111,500 elements (ne), and a close-up view

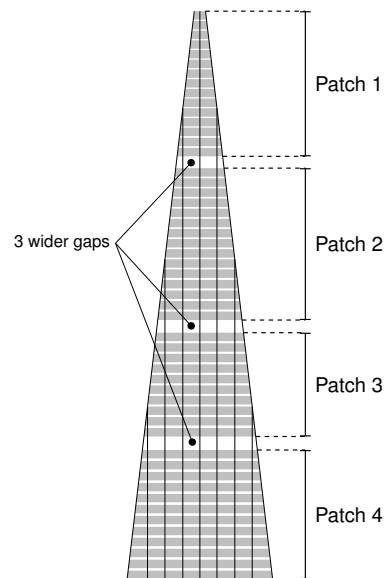


Figure 4.4: Patch definition (from [35, 34])

Table 4.2: Number of control points (nn) and number of elements (ne) in meshes

	nn	ne
Structure mesh	91,612	19,826
Membrane		6,648
Cable		13,177
Single-gore fluid mesh	198,112	111,500
Full-canopy fluid mesh	223,934	116,248

with nonmatching interfaces so the number of control points and elements could be reduced and the total number of control points and elements for the mesh kept within reason. The mesh is moved like the single-gore mesh to obtain meshes for the other flight conditions.

The same boundaries are set as in the single-gore computations. The porosity is modeled using Eq. (2.19) and (2.23) where the β term accounts for the geometric porosity. First, the porosity parameters from [34] followed by the porosity parameters calculated from the single-gore results. Sutherland's Law is again used to model viscosity. Flight condition AM31 is computed first and later flight conditions use previous results as initial data to decrease the time for each computation. Computations are run with GMRES iterations varying starting with 10 and increased to 60 later, 3 nonlinear iterations, and a time step size of 2.0×10^{-4} s. Only flight condition AM31 was completed for this thesis.

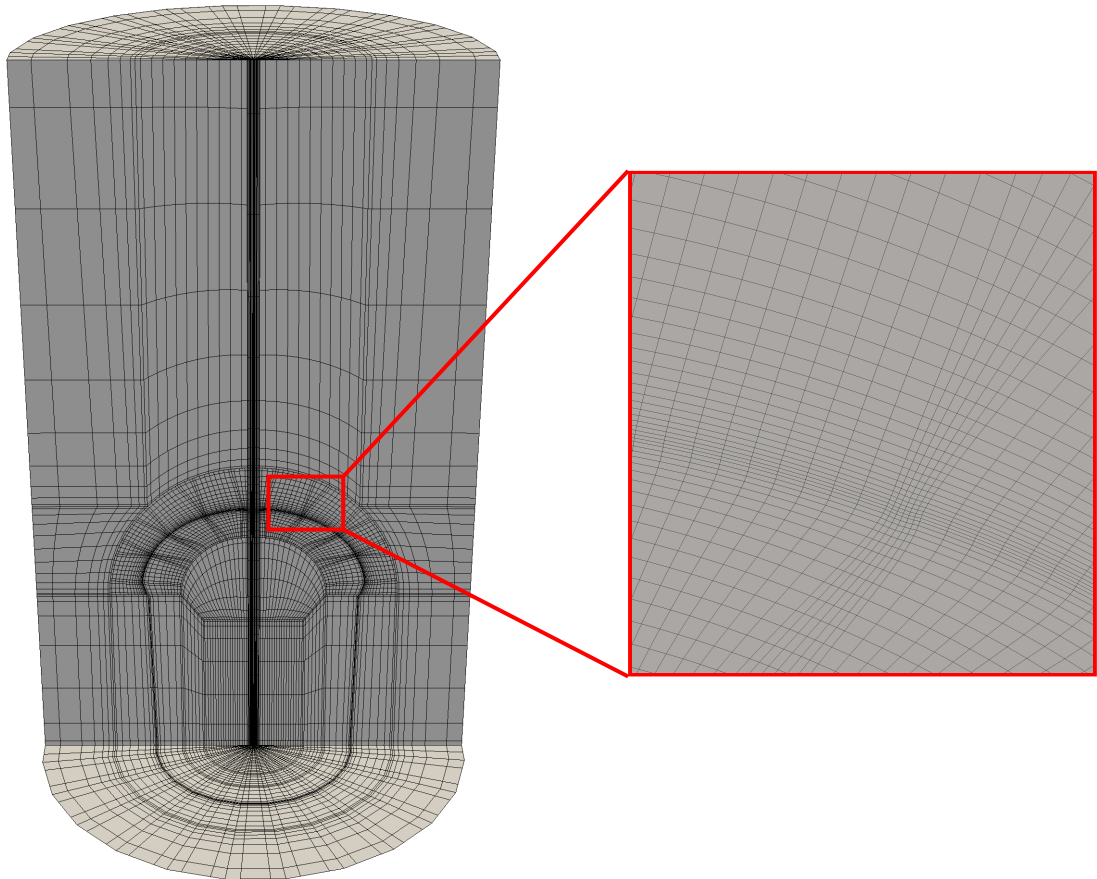


Figure 4.5: Fluid mechanics control mesh for AM31 full-canopy fluid computations with 223,934 control points (nn) and 116,248 elements (ne), and a close-up view

Chapter 5

Computational Results

5.1 Parachute Structure Results

Figure 5.1 shows the full parachute results for each flight condition. Although the results look similar, the parachute elongates more by a small amount with higher dynamic pressure as expected. The differences in diameter are also noted in Table 5.1 where the diameter is largest for AM13, the highest dynamic pressure, and smallest for AM31, the lowest dynamic pressure. The results are similar to previous computations by the T★AFSM using FEM meshes.

The area ratios of the fabric area and slits area, referred to by the subscript F and G respectively, to the combined area, referred to by the subscript 1, for the patches are shown in Table 5.2. The area ratios will be discussed later when they are used for modeling the porosity for the full-canopy computations. Generally, the fabric area ratio for each patch increased with higher dynamic pressure except Patch 4 for flight condition AM22. While the results are assumed to be steady, there is a slight breathing motion near the skirt which may account for this.

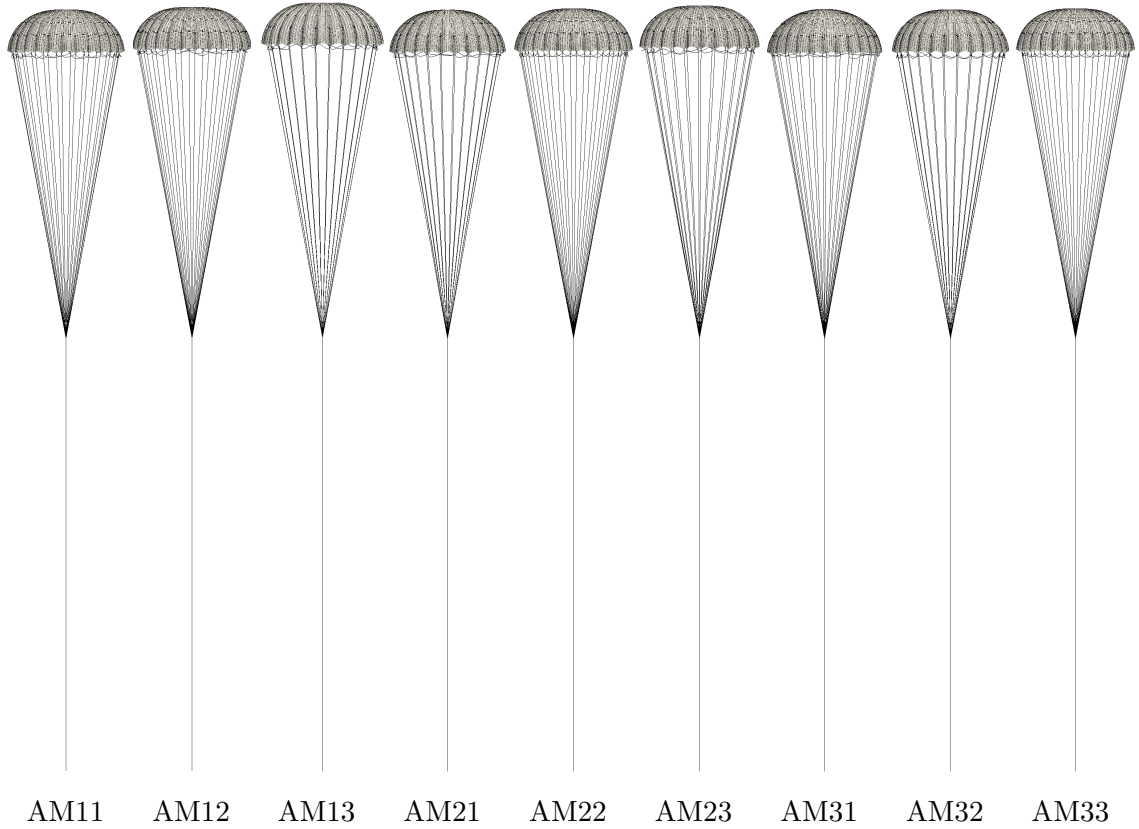


Figure 5.1: Structural mechanics parachute deformations

Table 5.1: Deformed parachute diameters

	D (ft)	D/D_0 (%)
D_0	23.0	100.0
AM11	17.8	77.2
AM12	18.1	78.8
AM13	18.6	80.7
AM21	17.6	76.5
AM22	17.9	78.0
AM23	18.2	79.2
AM31	17.4	75.8
AM32	17.8	77.2
AM33	18.0	78.1

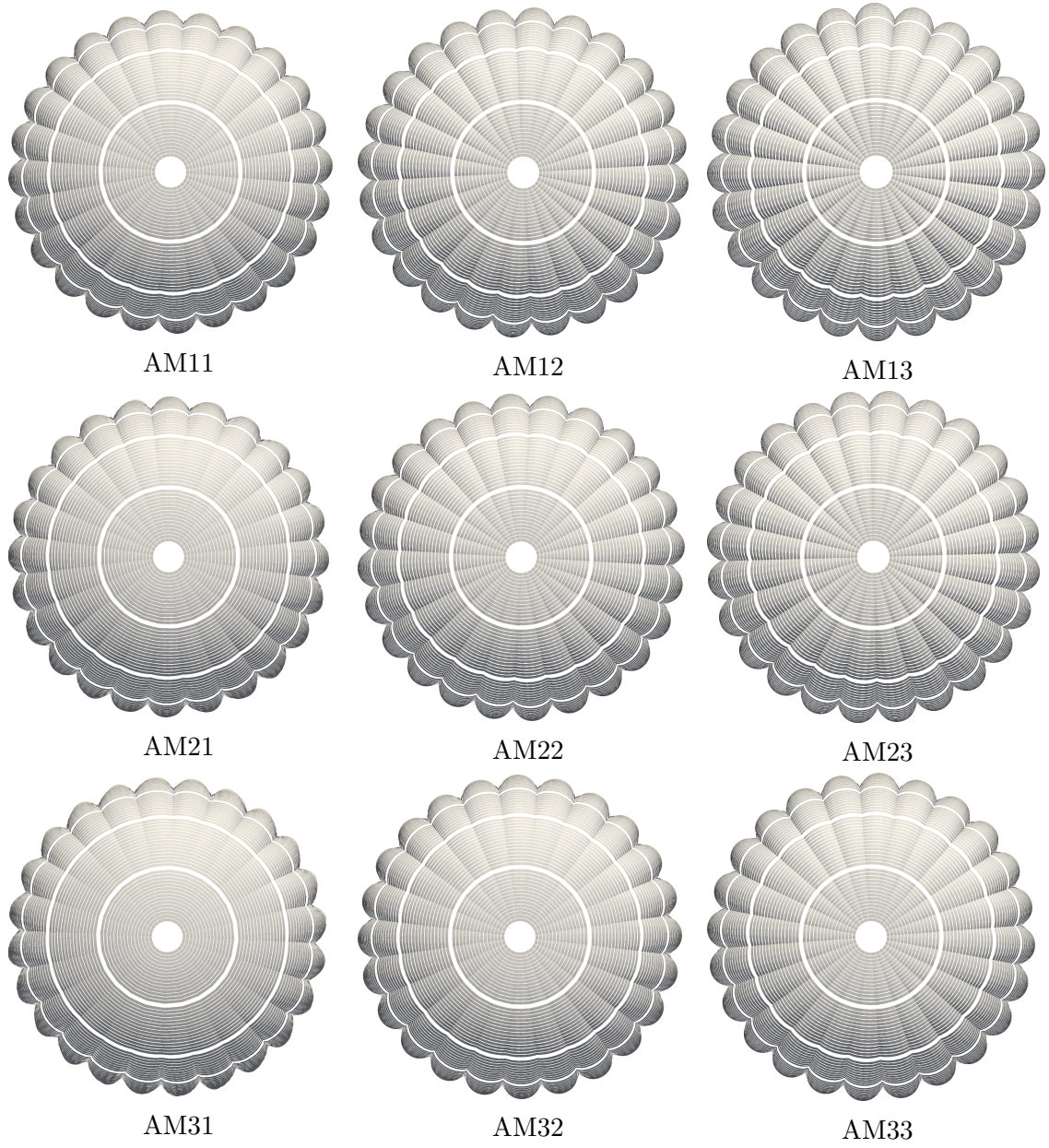


Figure 5.2: Canopy shape from structural mechanics computations looking in the vertical direction

Table 5.2: Fabric and geometric area ratios for each patch

	Patch	A_F/A_1	A_G/A_1		A_F/A_1	A_G/A_1		A_F/A_1	A_G/A_1
AM11	1	0.854	0.146	AM12	0.849	0.151	AM13	0.842	0.158
	2	0.813	0.187		0.803	0.197		0.792	0.208
	3	0.796	0.204		0.782	0.218		0.766	0.234
	4	0.783	0.217		0.781	0.219		0.776	0.224
AM21	1	0.855	0.145	AM22	0.851	0.149	AM23	0.846	0.154
	2	0.816	0.184		0.808	0.192		0.799	0.201
	3	0.799	0.201		0.789	0.211		0.777	0.223
	4	0.782	0.218		0.783	0.217		0.780	0.220
AM31	1	0.856	0.144	AM32	0.854	0.146	AM33	0.851	0.149
	2	0.818	0.182		0.814	0.186		0.808	0.192
	3	0.801	0.199		0.796	0.204		0.789	0.211
	4	0.770	0.230		0.782	0.218		0.782	0.218

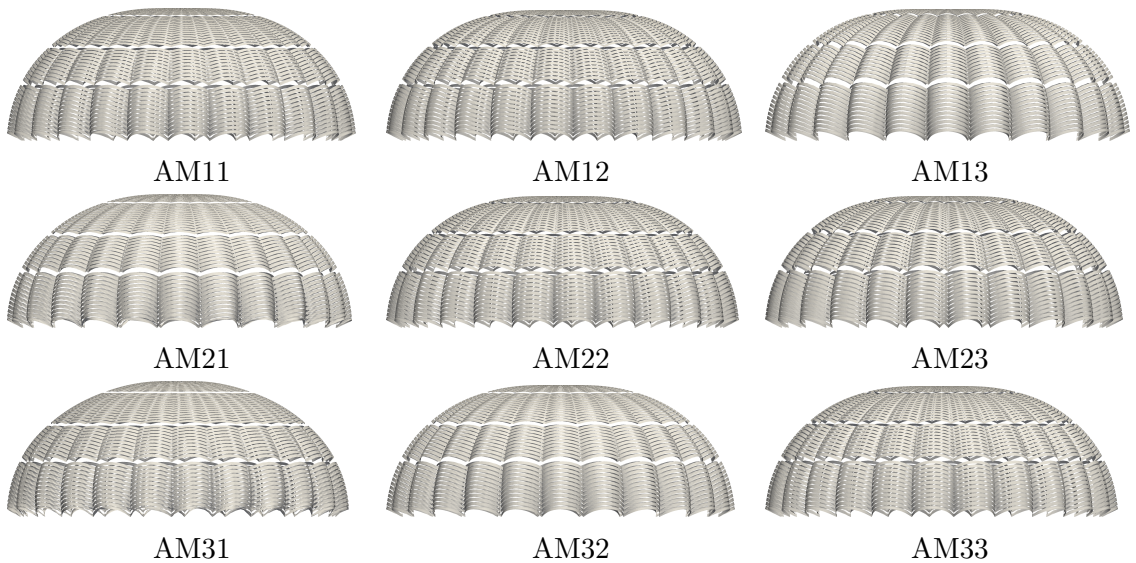


Figure 5.3: Canopy shape from structural mechanics computations looking in the y-direction

5.2 Single-Gore Fluid Results

Using the adiabatic porosity model, Figure 5.4 shows the mass flow through the the gaps as a function of time. As seen in previous FEM computations, the mass flow increases while Mach number increases and altitude decreases. The same trend is seen in Figure 5.5 for \mathcal{M}^2 . A least-squares curve fitting is applied to the final values $|\dot{m}|$ and \mathcal{M}^2 shown in Figure 5.4 and Figure 5.5, where the output coefficients are $\frac{\mu}{D}$ and β from Eq. (2.19) and (2.23) for the geometric part of the porosity model. Figure 5.6 shows graphically the results of the curve fitting while Table 5.3 lists the coefficients obtained along with the correlation factor.

Note that only flight conditions AM11, AM31, and AM32 were completed for this analysis. Other cases with higher dynamic pressures were not completed. The results from the computed flight conditions have a similar trend to the previous FEM results, but the values for the NURBS calculations tend to be lower for $|\dot{m}|$. This becomes apparent in the coefficient β which is almost double the values previously obtained. Because the total porosity is split between the fabric and geometric parts according to the equation

$$\begin{aligned}\mathcal{M}^2 &= \frac{\mu}{D}|\dot{m}| + \beta|\dot{m}|^2, \\ &= \left(\frac{A_F}{A_1} \left(\frac{\mu}{D} \right)_F + \frac{A_G}{A_1} \left(\frac{\mu}{D} \right)_G \right) |\dot{m}| + \left(\frac{A_F}{A_1} \beta_F + \frac{A_G}{A_1} \beta_G \right) |\dot{m}|^2, \quad (5.1)\end{aligned}$$

the differences are not as apparent for $\frac{\mu}{D}$ because the fabric property dominates both because of its large value compared to the $\left(\frac{\mu}{D} \right)_G$ and the area ratio also being larger. This is not the case for the β term because the fabric portion does not contribute to it. The calculated porosity parameters for the gaps are shown in Table 5.3 along with the coefficients of determination. Figure 5.7, Table 5.5, and Table 5.6 summarize the differences between the two results.

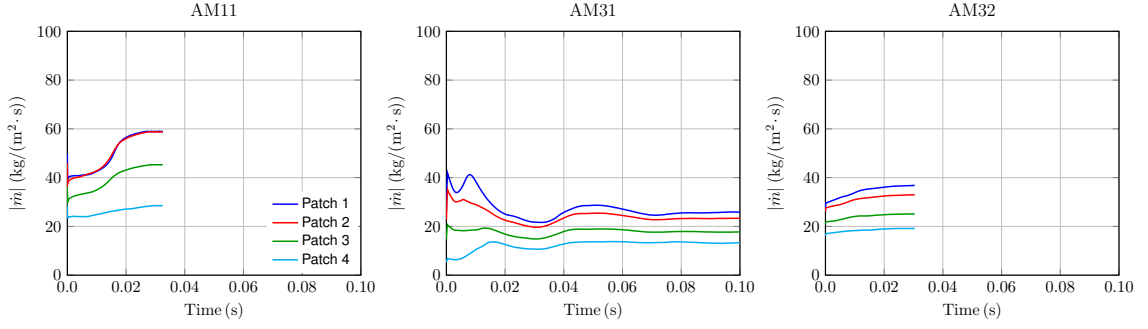
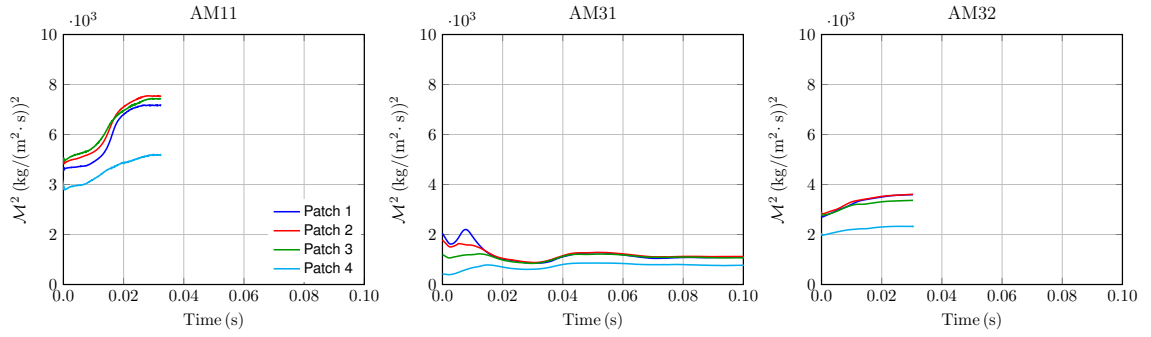
Figure 5.4: Patch-averaged values of $|\dot{m}|$ through the gapsFigure 5.5: Patch-averaged values of \mathcal{M}^2

Table 5.3: Calculated geometric porosity parameters

Patch	$(\frac{\mu}{D})_G$ (kg/(m ² · s))	β_G (-)	R ²
1	15.5	1.84	0.991
2	39.6	1.55	0.989
3	44.5	2.69	0.990
4	0	7.89	0.998

Table 5.4: Geometric porosity parameters from [34]

Patch	$(\frac{\mu}{D})_G$ (kg/(m ² · s))	β_G (-)	R ²
1	30.0	0.97	0.999
2	21.6	1.02	0.999
3	13.5	1.17	0.999
4	0	3.08	0.891

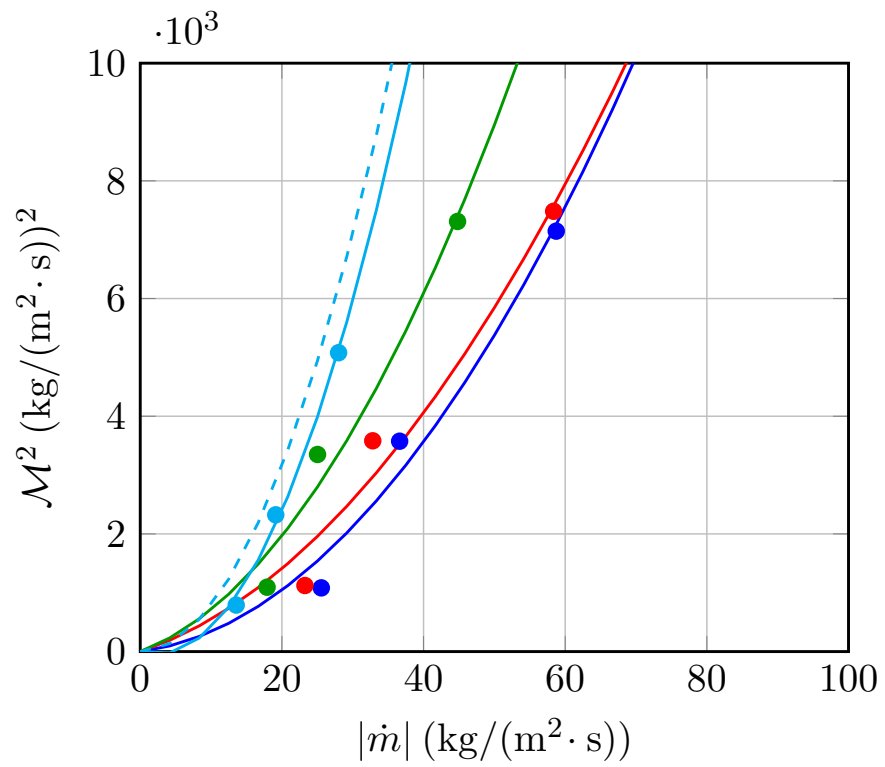


Figure 5.6: Patch-averaged values of $|\dot{m}|$, \mathcal{M}^2 , and \mathcal{M}^2 with the least-squares curve fitting lines where the dashed line for Patch 4 excludes the $\frac{\mu}{D}$ because it results in negative values for some \mathcal{M}^2

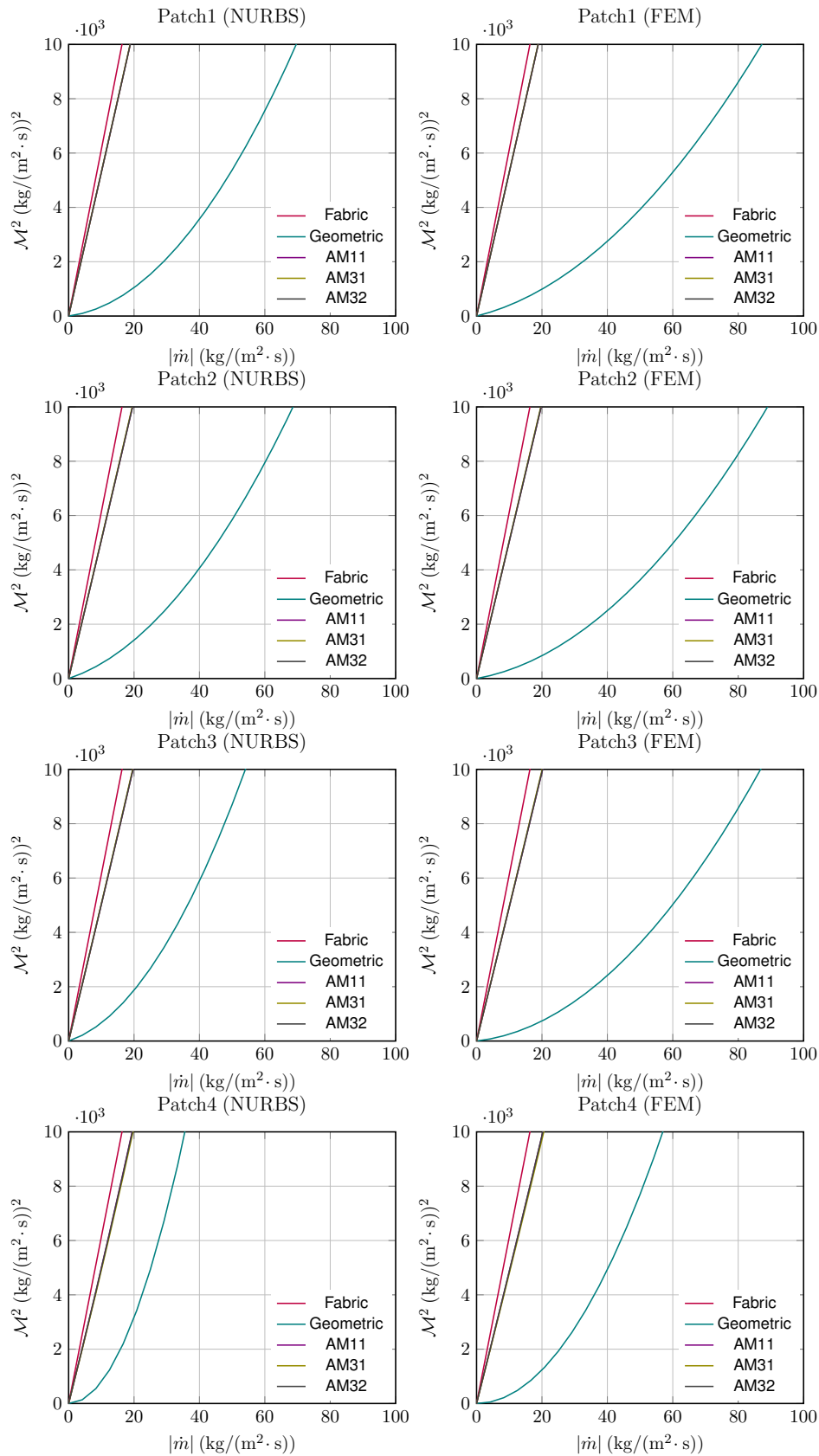


Figure 5.7: Comparison between using the parameters from the NURBS results and previous FEM results for \mathcal{M}^2 and $|\dot{m}|$ for each patch with the NURBS results on the left and FEM results on the right

Table 5.5: Porosity values from NURBS single-gore results

	Patch	$\frac{\mu}{D}$ (kg/(m ² · s))	β (-)	μ ($\times 10^{-5}$ Pa · s)	D ($\times 10^{-8}$ m)
AM11	1	525.5	0.269	1.69	3.22
	2	505.7	0.289		3.34
	3	496.6	0.549		3.41
	4	479.5	1.717		3.53
AM31	1	527.0	0.264	1.43	2.72
	2	508.7	0.281		2.82
	3	499.8	0.534		2.87
	4	471.8	1.816		3.04
AM32	1	525.6	0.269	1.43	2.73
	2	505.9	0.288		2.83
	3	496.9	0.548		2.89
	4	479.4	1.718		2.99

Table 5.6: Porosity values from [34] applied to new NURBS mesh

	Patch	$\frac{\mu}{D}$ (kg/(m ² · s))	β (-)	μ ($\times 10^{-5}$ Pa · s)	D ($\times 10^{-8}$ m)
AM11	1	527.3	0.142	1.69	3.24
	2	502.4	0.190		3.40
	3	490.3	0.239		3.49
	4	479.5	0.670		3.56
AM31	1	529.1	0.139	1.43	2.74
	2	505.4	0.185		2.86
	3	493.6	0.233		2.93
	4	471.8	0.708		3.07
AM32	1	527.7	0.142	1.43	2.74
	2	502.6	0.190		2.88
	3	490.6	0.239		2.95
	4	479.4	0.670		3.02

5.3 Full-Canopy Fluid Results

The full-canopy computations modeled the porosity according to Eqs. (2.19) and (2.23) accounting for the area ratios by Eq. (5.1). The computations are first run using the porosity coefficients obtained in earlier studies by the T★AFSM in [34] and shown in Table 5.6 after applying Eq. (5.1). Despite the seemingly large differences in β between the two cases, the results are very similar as seen in Figure 5.8, Figure 5.9 and 5.10.

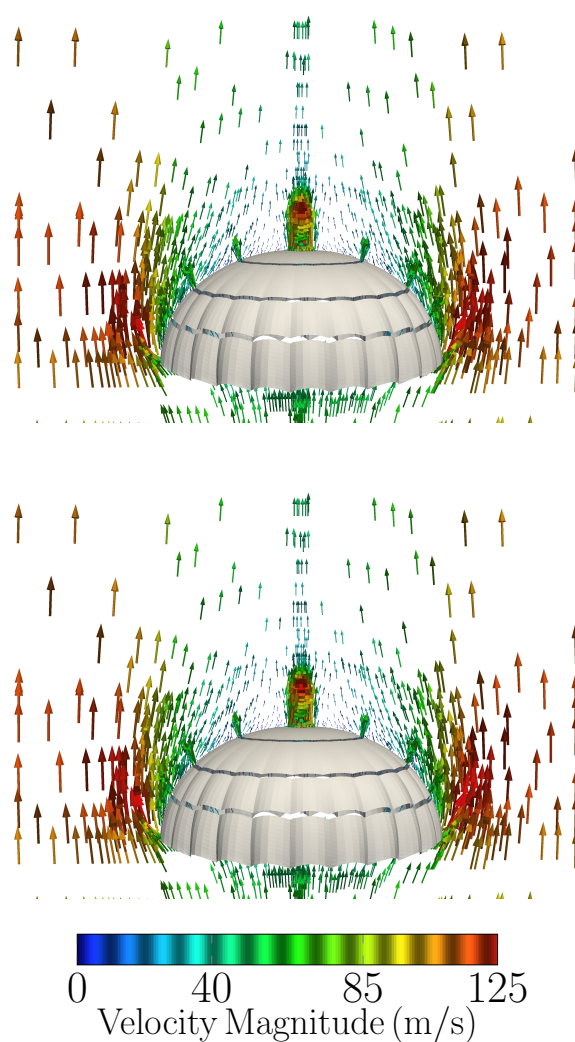


Figure 5.8: Velocity vectors around the canopy on a vertical slice plane scaled and colored to magnitude for AM31 using porosity parameters obtained from FEM on top and those obtained by NURBS below

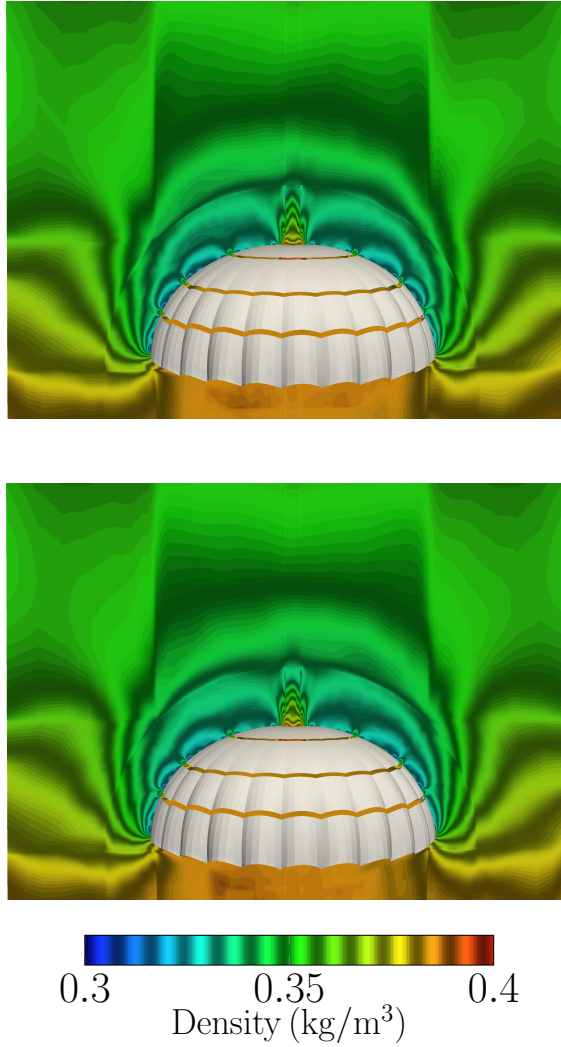


Figure 5.9: Density around the canopy on a vertical slice plane for AM31 using porosity parameters obtained from FEM on top and those obtained by NURBS below

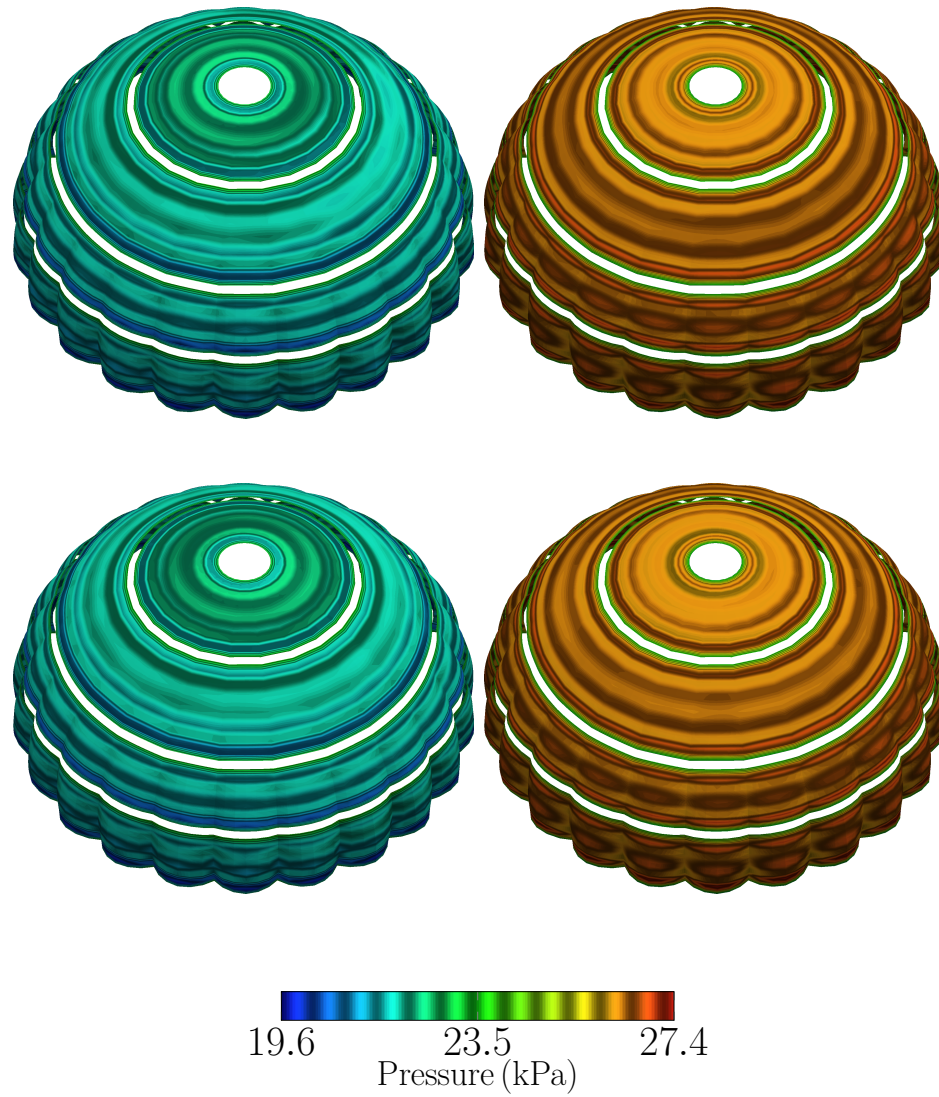


Figure 5.10: Pressure distribution above the canopy (left) and pressure distribution below the canopy (right) for AM31 using porosity parameters obtained from FEM on top and those obtained by NURBS below

Chapter 6

Concluding Remarks

Parachutes pose particular challenges that can be addressed as demonstrated by the computations and results in this thesis. Specifically, the use of IGA discretization can be used to successfully model the drogue parachute allowing for greater accuracy while limiting the computing resources necessary.

First, an initial parachute shape using a NURBS mesh was computed with the dynamic pressure for each flight conditions. The deformed shapes were used to make high resolution NURBS fluid meshes to calculate the geometric part of the porosity model. Full-gore fluid computations were then computed to obtain a starting flow field for future FSI computations. This thesis shows that IGA discretization is useful, practical, and accurate for use with the Orion drogue parachute and the porosity model used. This will be useful for future FSI research on the drogue parachute.

Bibliography

- [1] D. N. Arnold. An interior penalty finite element method with discontinuous elements. *SIAM Journal on Numerical Analysis*, 19:742–760, 1982.
- [2] Y. Bazilevs and I. Akkerman. Large eddy simulation of turbulent Taylor–Couette flow using isogeometric analysis and the residual–based variational multiscale method. *Journal of Computational Physics*, 229:3402–3414, 2010.
- [3] Y. Bazilevs, V. M. Calo, J. A. Cottrell, T. J. R. Hughes, A. Reali, and G. Scovazzi. Variational multiscale residual-based turbulence modeling for large eddy simulation of incompressible flows. *Computer Methods in Applied Mechanics and Engineering*, 197:173–201, 2007.
- [4] Y. Bazilevs, V. M. Calo, T. J. R. Hughes, and Y. Zhang. Isogeometric fluid–structure interaction: theory, algorithms, and computations. *Computational Mechanics*, 43:3–37, 2008.
- [5] Y. Bazilevs, V. M. Calo, Y. Zhang, and T. J. R. Hughes. Isogeometric fluid–structure interaction analysis with applications to arterial blood flow. *Computational Mechanics*, 38:310–322, 2006.
- [6] Y. Bazilevs and T. J. R. Hughes. NURBS-based isogeometric analysis for the computation of flows about rotating components. *Computational Mechanics*, 43:143–150, 2008.

- [7] Y. Bazilevs, K. Takizawa, and T. E. Tezduyar. *Computational Fluid–Structure Interaction: Methods and Applications*. Wiley, February 2013.
- [8] R. J. Benney, K. R. Stein, J. W. Leonard, and M. L. Accorsi. Current 3-D structural dynamic finite element modeling capabilities. In *Proceedings of AIAA 14th Aerodynamic Decelerator Systems Technology Conference*, AIAA Paper 97-1506, San Francisco, California, 1997.
- [9] A. N. Brooks and T. J. R. Hughes. Streamline upwind/Petrov-Galerkin formulations for convection dominated flows with particular emphasis on the incompressible Navier-Stokes equations. *Computer Methods in Applied Mechanics and Engineering*, 32:199–259, 1982.
- [10] R. Hartmann and P. Houston. An optimal order interior penalty discontinuous Galerkin discretization of the compressible Navier–Stokes equations. *Journal of Computational Physics*, 227:9670–9685, 2008.
- [11] H. M. Hilber, T. J. R. Hughes, and R. L. Taylor. Improved numerical dissipation for time integration algorithms in structural dynamics. *Earthquake Engineering and Structural Dynamics*, 5:283–292, 1977.
- [12] T. J. R. Hughes. Multiscale phenomena: Green’s functions, the Dirichlet-to-Neumann formulation, subgrid scale models, bubbles, and the origins of stabilized methods. *Computer Methods in Applied Mechanics and Engineering*, 127:387–401, 1995.
- [13] T. J. R. Hughes, J. A. Cottrell, and Y. Bazilevs. Isogeometric analysis: CAD, finite elements, NURBS, exact geometry, and mesh refinement. *Computer Methods in Applied Mechanics and Engineering*, 194:4135–4195, 2005.

- [14] T. J. R. Hughes and T. E. Tezduyar. Finite element methods for first-order hyperbolic systems with particular emphasis on the compressible Euler equations. *Computer Methods in Applied Mechanics and Engineering*, 45:217–284, 1984.
- [15] G. J. Le Beau, S. E. Ray, S. K. Aliabadi, and T. E. Tezduyar. SUPG finite element computation of compressible flows with the entropy and conservation variables formulations. *Computer Methods in Applied Mechanics and Engineering*, 104:397–422, 1993.
- [16] G. J. Le Beau and T. E. Tezduyar. Finite element computation of compressible flows with the SUPG formulation. In *Advances in Finite Element Analysis in Fluid Dynamics*, FED-Vol.123, pages 21–27, New York, 1991. ASME.
- [17] A. Lo. *Nonlinear Dynamic Analysis of Cable and Membrane Structure*. PhD thesis, Department of Civil Engineering, Oregon State University, 1982.
- [18] F. Rispoli, G. Delibra, P. Venturini, A. Corsini, R. Saavedra, and T. E. Tezduyar. Particle tracking and particle–shock interaction in compressible-flow computations with the V-SGS stabilization and $YZ\beta$ shock-capturing. *Computational Mechanics*, 55:1201–1209, 2015.
- [19] F. Rispoli, R. Saavedra, A. Corsini, and T. E. Tezduyar. Computation of inviscid compressible flows with the V-SGS stabilization and $YZ\beta$ shock-capturing. *International Journal for Numerical Methods in Fluids*, 54:695–706, 2007.
- [20] B. Riviere, M. F. Wheeler, and V. Girault. A priori error estimates for finite element methods based on discontinuous approximation spaces for elliptic problems. *SIAM Journal on Numerical Analysis*, 39:902–931, 2001.
- [21] K. Stein, R. Benney, V. Kalro, T. E. Tezduyar, J. Leonard, and M. Accorsi. Parachute fluid–structure interactions: 3-D Computation. *Computer Methods in Applied Mechanics and Engineering*, 190:373–386, 2000.

- [22] K. Takizawa, M. Fritze, D. Montes, T. Spielman, and T. E. Tezduyar. Fluid–structure interaction modeling of ringsail parachutes with disreefing and modified geometric porosity. *Computational Mechanics*, 50:835–854, 2012.
- [23] K. Takizawa, D. Montes, M. Fritze, S. McIntyre, J. Boben, and T. E. Tezduyar. Methods for FSI modeling of spacecraft parachute dynamics and cover separation. *Mathematical Models and Methods in Applied Sciences*, 23:307–338, 2013.
- [24] K. Takizawa, C. Moorman, S. Wright, J. Christopher, and T. E. Tezduyar. Wall shear stress calculations in space–time finite element computation of arterial fluid–structure interactions. *Computational Mechanics*, 46:31–41, 2010.
- [25] K. Takizawa, C. Moorman, S. Wright, T. Spielman, and T. E. Tezduyar. Fluid–structure interaction modeling and performance analysis of the Orion spacecraft parachutes. *International Journal for Numerical Methods in Fluids*, 65:271–285, 2011.
- [26] K. Takizawa, T. Spielman, and T. E. Tezduyar. Space–time FSI modeling and dynamical analysis of spacecraft parachutes and parachute clusters. *Computational Mechanics*, 48:345–364, 2011.
- [27] K. Takizawa and T. E. Tezduyar. Multiscale space–time fluid–structure interaction techniques. *Computational Mechanics*, 48:247–267, 2011.
- [28] K. Takizawa and T. E. Tezduyar. Computational methods for parachute fluid–structure interactions. *Archives of Computational Methods in Engineering*, 19:125–169, 2012.
- [29] K. Takizawa and T. E. Tezduyar. Space–time fluid–structure interaction methods. *Mathematical Models and Methods in Applied Sciences*, 22(supp02):1230001, 2012.

- [30] K. Takizawa, T. E. Tezduyar, J. Boben, N. Kostov, C. Boswell, and A. Buscher. Fluid–structure interaction modeling of clusters of spacecraft parachutes with modified geometric porosity. *Computational Mechanics*, 52:1351–1364, 2013.
- [31] K. Takizawa, T. E. Tezduyar, C. Boswell, R. Kolesar, and K. Montel. FSI modeling of the reefed stages and disreefing of the Orion spacecraft parachutes. *Computational Mechanics*, 54:1203–1220, 2014.
- [32] K. Takizawa, T. E. Tezduyar, and A. Buscher. Space–time computational analysis of MAV flapping-wing aerodynamics with wing clapping. *Computational Mechanics*, 55:1131–1141, 2015.
- [33] K. Takizawa, T. E. Tezduyar, A. Buscher, and S. Asada. Space–time fluid mechanics computation of heart valve models. *Computational Mechanics*, 54:973–986, 2014.
- [34] K. Takizawa, T. E. Tezduyar, and T. Kanai. Porosity models and computational methods for compressible-flow aerodynamics of parachutes with geometric porosity. *Mathematical Models and Methods in Applied Sciences*, published online, DOI: 10.1142/S0218202517500166, March 2017.
- [35] K. Takizawa, T. E. Tezduyar, and R. Kolesar. FSI modeling of the Orion spacecraft drogue parachutes. *Computational Mechanics*, 55:1167–1179, 2015.
- [36] K. Takizawa, T. E. Tezduyar, R. Kolesar, C. Boswell, T. Kanai, and K. Montel. Multiscale methods for gore curvature calculations from FSI modeling of spacecraft parachutes. *Computational Mechanics*, 54:1461–1476, 2014.
- [37] K. Takizawa, T. E. Tezduyar, H. Mochizuki, H. Hattori, S. Mei, L. Pan, and K. Montel. Space–time VMS method for flow computations with slip interfaces (ST-SI). *Mathematical Models and Methods in Applied Sciences*, 25:2377–2406, 2015.

- [38] K. Takizawa, T. E. Tezduyar, Y. Otoguro, T. Terahara, T. Kuraishi, and H. Hattori. Turbocharger flow computations with the Space–Time Isogeometric Analysis (ST-IGA). *Computers & Fluids*, 142:15–20, 2017.
- [39] K. Takizawa, S. Wright, C. Moorman, and T. E. Tezduyar. Fluid–structure interaction modeling of parachute clusters. *International Journal for Numerical Methods in Fluids*, 65:286–307, 2011.
- [40] T. Tezduyar, S. Aliabadi, M. Behr, A. Johnson, V. Kalro, and M. Litke. Flow simulation and high performance computing. *Computational Mechanics*, 18:397–412, 1996.
- [41] T. E. Tezduyar. Stabilized finite element formulations for incompressible flow computations. *Advances in Applied Mechanics*, 28:1–44, 1992.
- [42] T. E. Tezduyar. Finite element methods for flow problems with moving boundaries and interfaces. *Archives of Computational Methods in Engineering*, 8:83–130, 2001.
- [43] T. E. Tezduyar. Computation of moving boundaries and interfaces and stabilization parameters. *International Journal for Numerical Methods in Fluids*, 43:555–575, 2003.
- [44] T. E. Tezduyar. Finite element methods for fluid dynamics with moving boundaries and interfaces. In E. Stein, R. D. Borst, and T. J. R. Hughes, editors, *Encyclopedia of Computational Mechanics*, Volume 3: Fluids, chapter 17. Wiley, 2004.
- [45] T. E. Tezduyar. Finite elements in fluids: Special methods and enhanced solution techniques. *Computers & Fluids*, 36:207–223, 2007.

- [46] T. E. Tezduyar. Finite elements in fluids: Stabilized formulations and moving boundaries and interfaces. *Computers & Fluids*, 36:191–206, 2007.
- [47] T. E. Tezduyar, S. K. Aliabadi, M. Behr, and S. Mittal. Massively parallel finite element simulation of compressible and incompressible flows. *Computer Methods in Applied Mechanics and Engineering*, 119:157–177, 1994.
- [48] T. E. Tezduyar, M. Behr, and J. Liou. A new strategy for finite element computations involving moving boundaries and interfaces – the deforming-spatial-domain/space–time procedure: I. The concept and the preliminary numerical tests. *Computer Methods in Applied Mechanics and Engineering*, 94(3):339–351, 1992.
- [49] T. E. Tezduyar, M. Behr, S. Mittal, and J. Liou. A new strategy for finite element computations involving moving boundaries and interfaces – the deforming-spatial-domain/space–time procedure: II. Computation of free-surface flows, two-liquid flows, and flows with drifting cylinders. *Computer Methods in Applied Mechanics and Engineering*, 94(3):353–371, 1992.
- [50] T. E. Tezduyar and T. J. R. Hughes. Finite element formulations for convection dominated flows with particular emphasis on the compressible Euler equations. In *Proceedings of AIAA 21st Aerospace Sciences Meeting*, AIAA Paper 83-0125, Reno, Nevada, 1983.
- [51] T. E. Tezduyar and S. Sathe. Modeling of fluid–structure interactions with the space–time finite elements: Solution techniques. *International Journal for Numerical Methods in Fluids*, 54:855–900, 2007.
- [52] T. E. Tezduyar, S. Sathe, T. Cragin, B. Nanna, B. S. Conklin, J. Pausewang, and M. Schwaab. Modeling of fluid–structure interactions with the space–time

- finite elements: Arterial fluid mechanics. *International Journal for Numerical Methods in Fluids*, 54:901–922, 2007.
- [53] T. E. Tezduyar, S. Sathe, R. Keedy, and K. Stein. Space–time finite element techniques for computation of fluid–structure interactions. *Computer Methods in Applied Mechanics and Engineering*, 195:2002–2027, 2006.
- [54] T. E. Tezduyar, S. Sathe, J. Pausewang, M. Schwaab, J. Christopher, and J. Crabtree. Interface projection techniques for fluid–structure interaction modeling with moving-mesh methods. *Computational Mechanics*, 43:39–49, 2008.
- [55] T. E. Tezduyar, S. Sathe, M. Schwaab, J. Pausewang, J. Christopher, and J. Crabtree. Fluid–structure interaction modeling of ringsail parachutes. *Computational Mechanics*, 43:133–142, 2008.
- [56] T. E. Tezduyar and M. Senga. Stabilization and shock-capturing parameters in SUPG formulation of compressible flows. *Computer Methods in Applied Mechanics and Engineering*, 195:1621–1632, 2006.
- [57] T. E. Tezduyar and M. Senga. SUPG finite element computation of inviscid supersonic flows with $YZ\beta$ shock-capturing. *Computers & Fluids*, 36:147–159, 2007.
- [58] T. E. Tezduyar, M. Senga, and D. Vicker. Computation of inviscid supersonic flows around cylinders and spheres with the SUPG formulation and $YZ\beta$ shock-capturing. *Computational Mechanics*, 38:469–481, 2006.
- [59] T. E. Tezduyar, K. Takizawa, C. Moorman, S. Wright, and J. Christopher. Space–time finite element computation of complex fluid–structure interactions. *International Journal for Numerical Methods in Fluids*, 64:1201–1218, 2010.